Appendix

Appendix A

Secondary Organic Aerosol Formation from Isoprene Photooxidation*

---

*This chapter is reproduced by permission from "Secondary organic aerosol formation from isoprene photooxidation" by J. H. Kroll, N. L. Ng, S. M. Murphy, R. C. Flagan, J. H. Seinfeld, A. Lee., and A. H.Goldstein, *Environmental Science and Technology*, 40, 1869-1877, 2006. Copyright 2006. American Chemical Society.

Environ. Sci. Technol. **2006**, *40,* 1869−1877

Secondary Organic Aerosol Formation from Isoprene Photooxidation

JESSE H. KROLL, NGA L. NG,
SHANE M. MURPHY,
RICHARD C. FLAGAN, AND
JOHN H. SEINFELD*

Departments of Environmental Science and Engineering and Chemical Engineering, California Institute of Technology, Pasadena, California 91125

Recent work has shown that the atmospheric oxidation of isoprene (2-methyl-1,3-butadiene, C_5H_8) leads to the formation of secondary organic aerosol (SOA). In this study, the mechanism of SOA formation by isoprene photooxidation is comprehensively investigated, by measurements of SOA yields over a range of experimental conditions, namely isoprene and NO_x concentrations. Hydrogen peroxide is used as the radical precursor, substantially constraining the observed gas-phase chemistry; all oxidation is dominated by the OH radical, and organic peroxy radicals (RO_2) react only with HO_2 (formed in the OH + H_2O_2 reaction) or NO concentrations, including NO_x-free conditions. At high NO_x, yields are found to decrease substantially with increasing [NO_x], indicating the importance of RO_2 chemistry in SOA formation. Under low-NO_x conditions, SOA mass is observed to decay rapidly, a result of chemical reactions of semivolatile SOA components, most likely organic hydroperoxides.

Introduction

As a substantial fraction of tropospheric particulate matter (PM) is composed of organic material, a detailed understanding of the sources and sinks of condensed organic compounds in the atmosphere is necessary to understand the effects of PM on the earth's climate and human health. A major source of uncertainty is the formation of secondary organic aerosol (SOA), particulate matter that is not emitted into the troposphere directly but rather is formed by gas-to-particle conversion of the oxidation products of volatile organic compounds (VOC's). At present, the global formation of SOA is poorly constrained, with estimates from modeling studies ranging from 12 to 70 Tg/year (*1*). Such estimates rely critically on laboratory measurements of the amount of SOA produced by individual SOA precursors, typically carried out in large environmental (smog) chambers. From these yield measurements, coupled with atmospheric models, it is now understood that the dominant contributors to global SOA are biogenic hydrocarbons (terpenes and sesquiterpenes), which form SOA primarily by reaction with the hydroxyl radical (OH) and ozone (O_3) (*2*). Anthropogenic hydrocarbons (most notably aromatic compounds) are also believed to make a minor contribution to SOA on a global scale (*3*).

The global emission of biogenic terpenes and anthropogenic hydrocarbons is far lower than that of isoprene (2-methyl-1,3-butadiene, C_5H_8), estimated at ~500 Tg/year (*4*). Despite this large flux, isoprene has generally not been considered to be an SOA precursor, owing to the high volatility of its known reaction products. First-generation reaction products of the OH-isoprene reaction (under high-NO_x conditions) are well-characterized, with a measured carbon balance approaching 100%; structures and yields are shown in Figure 1. These products are too volatile to partition appreciably into the aerosol phase, and on this basis, isoprene is not expected to form SOA. Pandis et al. (*12*) and Edney et al. (*13*), for example, observed no aerosol growth from the photooxidation of isoprene under high-NO_x conditions.

Recent work suggests that isoprene may contribute to organic aerosol formation via heterogeneous reactions. Claeys and co-workers (*14*−*16*) have recently measured tetrols with the same carbon backbone as isoprene (as well as related compounds) in a number of atmospheric samples. Such species are likely to be formed by heterogeneous reactions; formation of tetrols has been observed in the aqueous-phase oxidation of isoprene in the presence of acid and hydrogen peroxide (*17*), as well as in the gas-phase photooxidation of isoprene in the presence of NO_x, SO_2, and ammonium sulfate seed (*13*). In the latter study only ~6% of the SOA mass observed could be identified (as tetrols and related products), suggesting the formation of other low-volatility compounds. In fact, Limbeck et al. showed (*18*) that polymeric, humic-like substances are formed when isoprene is passed through filters impregnated with sulfuric acid. Czoschke et al. (*19*) reported that the (very small) SOA yields from the ozonolysis of isoprene were enhanced in the presence of acidic seed particles, suggesting the polymerization of gas-phase oxidation reaction products as well. Matsunaga et al. (*20*, *21*) measured high concentrations of second-generation isoprene oxidation products (hydroxyacetone, methylglyoxal, and glycolaldehyde) in aerosol samples, which may also suggest heterogeneous reactions leading to enhanced uptake. Additionally, modeling studies (*22*, *23*) predict that water-soluble isoprene oxidation products will be scavenged by clouds, where they may be oxidized to lower-volatility compounds that remain in the condensed phase after droplet evaporation. Thus, isoprene may contribute to SOA via a number of heterogeneous chemical reactions, involving either polymerization or oxidation of isoprene and its reaction products.

In a recent study (*24*), we provided laboratory evidence that the gas-phase oxidation of isoprene indeed forms SOA. Isoprene oxidation was initiated by the photolysis of nitrous acid (HONO) in the presence of NO_x and ammonium sulfate seed, with SOA (yields of 0.9−3.0%) detected from isoprene concentrations as low as 60 ppb. At smaller concentrations, SOA yields could not be determined, due to the loss of particles to the walls, so SOA formation from isoprene oxidation under tropospheric conditions could not be determined. The difference in these results from those of Pandis et al. (*12*) and Edney et al. (*13*) likely arose from lower temperatures (20 °C vs 30 °C) and differences in oxidative conditions. SOA was shown to be formed from the oxidation of first-generation reaction products, but details of the underlying chemistry remain unclear. Many factors that may play a role in SOA formation have yet to be examined, such as reactions by different oxidants (OH, O_3, and NO_3), heterogeneous reactions (such as those outlined above), and NO_x concentration.

---

* Corresponding author phone: (626) 395-4635; fax: (626) 796-2591; e-mail: seinfeld@caltech.edu.

10.1021/es0524301 CCC: $33.50

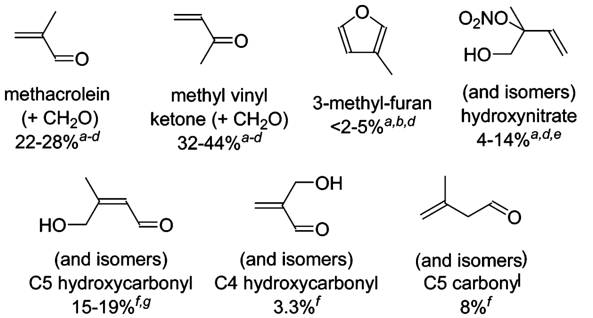

FIGURE 1. Structures and measured yields of first-generation products of the OH-initiated oxidation of isoprene under high-NO_x conditions. [a]Tuazon and Atkinson (*5*). [b]Paulson et al. (*6*). [c]Miyoshi et al. (*7*). [d]Sprengnether et al. (*8*). [e]Chen et al. (*9*). [f]Zhao et al. (*10*). [g]Baker et al. (*11*).

In the present study we examine SOA formation from isoprene in greater detail, to better understand the chemical mechanism of particle growth. The focus of this study is total SOA growth under varying reaction conditions (in particular NO_x and isoprene concentrations); the chemical composition of the SOA is beyond the scope of this work, and will be discussed in detail in a forthcoming paper. In these experiments, hydrogen peroxide (H_2O_2) is used as the radical precursor. H_2O_2 photolysis continually produces OH and HO_2 (from the OH + H_2O_2 reaction) over the course of the experiments, greatly simplifying the gas-phase chemistry. Gas-phase oxidation is dominated by reaction with OH (the primary oxidant of isoprene in the troposphere), with minimal interference by O_3 or NO_3. NO_x can be systematically varied over a wide range of concentrations by the addition of NO, and peroxy radical (RO_2) chemistry is relatively straightforward because any RO_2 formed will react only with HO_2 or NO. Additionally, here we use much lower seed particle loadings than in previous experiments, allowing for the precise measurement of small SOA volumes. From these measurements we are able to better constrain the chemical mechanism of SOA formation from isoprene oxidation, particularly the role of peroxy radicals.

Experimental Section

Experiments are carried out in Caltech's dual 28 m^3 FEP Teflon chambers, described in detail elsewhere (*25*, *26*). The chambers are surrounded by banks of blacklights (276 GE350BL) and aluminum sheets for maximum reflectivity. Numerous ports allow both for the introduction of clean air, gas-phase reagents, and inorganic seed, and for various gas-phase and particulate measurements. A differential mobility analyzer (DMA, TSI 3760) measures the size distribution and volume concentration of particles inside the chambers; settings are the same as described in Keywood et al. (*26*). In most experiments, an Aerodyne Time-of-Flight aerosol mass spectrometer (AMS, described in detail in ref. *27*) is also used, for the measurement of mass distributions of particulate organics, sulfate, nitrate, and ammonium. A gas chromatograph coupled with flame ionization detection (GC−FID, HP 5890) allows for the measurement of gas-phase isoprene. GC−FID response is calibrated by sampling from a 60 L FEP Teflon bag into which known volumes of isoprene have been introduced. Temperature, relative humidity (RH), O_3, NO, and NO_x are all continually monitored. Experiments are run in each chamber on alternating days; the chamber that is not in use on a given day is repeatedly flushed with clean air and irradiated with UV light for cleaning.

The radical precursor used in the present experiments is hydrogen peroxide. H_2O_2 is introduced by bubbling 5 L/min of humidified room-temperature air for 2 1/2 hours through a 50% H_2O_2 solution (Aldrich), through a particle filter to avoid the introduction of droplets, and finally into the chamber. The concentration of H_2O_2 is not measured directly, but from the rate of isoprene decay during irradiation, and literature values of $\sigma_{H_2O_2}$, $k_{\mathrm{OH+isoprene}}$, and $k_{\mathrm{OH+H_2O_2}}$ (*28*, *29*), $[H_2O_2]$ is estimated to be ∼3−5 ppm; this may decrease somewhat over the course of the experiment due to wall loss, photolysis, and reaction with OH. To minimize potential uptake of H_2O_2 into the particle phase, all experiments are run under dry (RH < 10%) conditions. These conditions are substantially drier than those of the troposphere. The dependence of SOA growth on RH is beyond the scope of this work but warrants future investigation.

After introduction of H_2O_2, ammonium sulfate seed (if used) is introduced by atomization of a 0.015 M solution of $(NH_4)_2SO_4$ at 30 psi; initial volume concentrations are 4.6−7.1 $\mu m^3/cm^3$. For high-NO_x experiments, a known quantity of NO is then introduced from a 500 ppm gas cylinder (in N_2, Scott Specialty Gases). Typically, some fraction (20−40 ppb) is immediately converted to NO_2, likely from reactions with residual O_3 and NO_3/N_2O_5 in the chamber, and so the chamber is free of any oxidants when hydrocarbon is added. Isoprene (12−90 ppb) is introduced by sending air over a measured volume of the pure compound (Aldrich, 99.8%) and into the chamber.

When all components are well-mixed (measured values of isoprene, NO_x, and seed particle volume are constant), the blacklights are turned on, initiating photooxidation and the beginning of the experiment. Output from the lights in the ultraviolet is between 300 and 400 nm, with a maximum at 354 nm. The very weak absorption cross section of H_2O_2 in this range necessitates the use of more lights than in our prior study using HONO (*24*); half the available lights are used in the present experiments. Using measurements of photon flux inside the chamber enclosure and known absorption cross sections (*28*), we calculate J_{NO_2} and $J_{\mathrm{HH_2O_2}}$ to be 0.29 $\min^{-1}$ and 0.00029 $\min^{-1}$, respectively; hence, ppm concentrations of H_2O_2 are required. Heating from the lights leads to a temperature increase inside the chamber of approximately 5 °C over the course of the experiment. The DMA and AMS are both located outside the chamber enclosure and are at the temperature of the surrounding room (∼20−22 °C). Thus, the air may cool slightly as it is sampled from the chamber and into the instruments, and the measured aerosol is likely to correspond to gas-particle partitioning at the temperature of the room rather than the temperature at which the gas-phase chemistry occurs. Such temperature differences (≤5 °C) are unlikely to affect results significantly.

Results

Blank Runs. To ensure that all SOA growth observed is indeed from isoprene photooxidation, blank runs are performed regularly over the course of the data collection. Minimal growth (<0.1 $\mu g/m^3$) is observed from irradiation of mixtures of H_2O_2, NO_x, and/or inorganic seed (with no isoprene present). In addition, from the measured SOA yields and mass spectra, the particle growth observed cannot be the result of a small terpene impurity (∼0.2%) in the isoprene. These results are described in detail in the Supporting Information.

Low-NO_x Experiments. Shown in Figure 2 is a typical low-NO_x experiment ($[NO_x]$ < 1 ppb), in which 63.6 ppb isoprene is oxidized in the absence of inorganic seed. Particles are detected after ∼40 min of irradiation; aerosol growth is measured using both the DMA and AMS and occurs mostly after all the isoprene has been reacted. AMS data confirm that the new particle mass is organic, with a typical mass spectrum shown in Figure 3. Ozone formation (not shown in Figure 2) of a few ppb is observed, possibly due to residual

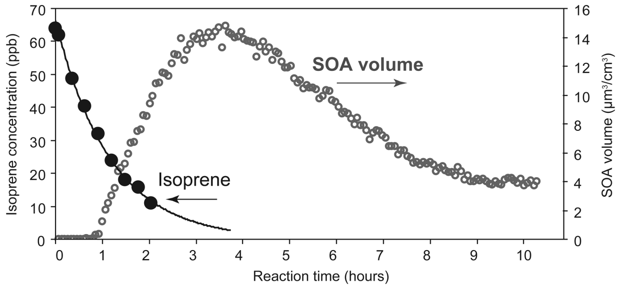

FIGURE 2. Reaction profile of a typical isoprene photooxidation experiment under NO_x-free conditions (Experiment 5).

NO_x emitted by the chamber walls. Such small O_3 concentrations are unlikely to have any appreciable effect on the gas-phase chemistry. After an initial period of aerosol growth, aerosol mass and volume are observed to decrease rapidly to lower final values. This is not a result of the loss of particles to the walls, as it is characterized by a shrinking of the aerosol size distribution rather than a decrease in number concentration. The loss of aerosol mass stops immediately when the lights are turned off, and resumes when the lights are turned back on, suggesting it is not caused by gradual changes in temperature or RH. Possible mechanisms are examined in the Discussion section.

Aerosol growth from isoprene photooxidation is also observed at lower isoprene concentrations (and, hence, smaller organic aerosol loadings). The DMA detects SOA from isoprene concentrations as low as 12.2 ppb; below that, the signal-to-noise is too poor for the detection of growth. Aerosol growth is detected at still lower isoprene concentrations (~8 ppb) by the AMS. The mass spectra of the SOA, at maximum growth and at the end of the experiment, are similar to those from the higher-concentration experiments, indicating that SOA formation is indeed significant, even at such low isoprene concentrations and particulate loadings.

Experimental conditions and results from all low-NO_x experiments are given in Table 1. For all these experiments, no inorganic seed is added; the small size of nucleated particles leads to good signal-to-noise of the DMA volume measurement so that very small growths (<1 $\mu m^3/cm^3$) can be measured. Measured increases in aerosol volume are found to be largely insensitive to the presence of ammonium sulfate seed. Two values for the increase in aerosol volume are given in Table 1: "maximum growth" (before the rapid loss of SOA dominates) and "final growth" (once SOA volume and mass have leveled out). All volumes are corrected for losses to the chamber walls, by applying size-dependent first-order loss coefficients, estimated by running "seed-only" experiments in the absence of hydrocarbon (*26*). SOA yield, defined as the ratio of mass concentration of SOA formed to mass concentration of isoprene reacted, is given for the final growth only. This requires knowledge of the SOA density, determined by a comparison of aerosol volume (from the DMA) and aerosol mass (from the AMS), as described by Bahreini et al. (*30*). Density is determined to be 1.25 (±0.1) g/cm^3 for SOA formed under low NO_x conditions. As is typical for SOA-forming reactions, yields are found to vary with the amount of hydrocarbon reacted (*31*, *32*); the dependence of aerosol growth (both maximum and final growth) on the amount of isoprene reacted is illustrated in Figure 4.

TABLE 1. Experimental Conditions and Results for NO_x-free Experiments[a]

expt. no.	isoprene reacted (ppb)	ΔM_o (max) ($\mu g/m^3$)[b]	ΔM_o (final) ($\mu g/m^3$)[b]	SOA yield (%)[c]	T_{max} (°C)
1	90.0	27.0 ± 0.5	9.3 ± 0.4	3.6 ± 0.1	25.4
2	46.1	13.5 ± 0.6	3.8 ± 0.5	2.9 ± 0.3	25.6
3	23.0	2.3 ± 0.5	0.6 ± 0.3	0.9 ± 0.4	26.0
4	12.2	0.7 ± 0.1	0.3 ± 0.1	1.0 ± 0.3	25.7
5	63.6	17.8 ± 0.5	5.0 ± 0.5	2.8 ± 0.3	26.7
6	29.4	6.2 ± 0.8	2.2 ± 0.5	2.6 ± 0.6	28.7
7	47.8	11.1 ± 0.5	3.0 ± 0.4	2.2 ± 0.3	26.6
8	41.6	8.4 ± 0.4	2.4 ± 0.5	2.1 ± 0.5	26.4

[a] Stated uncertainties (2σ) are from scatter in particle volume measurements. [b] Assuming an SOA density of 1.25 g/cm^3. [c] SOA yields from final growth only.

High-NO_x Experiments. The addition of NO to the reaction mixture has a large effect on the gas-phase chemistry, as illustrated in Figure 5 for a typical experiment (42.7 ppb isoprene, 98 ppb NO, 31 ppb NO_2, 6.4 $\mu m^3/m^3$ seed). Isoprene decay is far faster than in the low-NO_x case, due to regeneration of OH from the HO_2 + NO reaction. This reaction also rapidly converts NO to NO_2. Ozone formation, from NO_2 photolysis, begins once [NO] falls below ~50 ppb. When [NO] approaches zero (concentrations of a few ppb), aerosol growth is observed. Aerosol mass and volume typically reach a maximum after ~4 h into the reaction; unlike in the low-NO_x case, no rapid loss of SOA is observed.

The mass spectrum of SOA formed from isoprene under typical high-NO_x conditions is shown in Figure 6. SOA composition is clearly different from that formed under NO_x-free conditions (Figure 3), with mass fragments displaying a more ordered, repetitive pattern. Aerosol growth is also observed from the oxidation of ~8 ppb isoprene (with 280 ppb NO); the mass spectrum is again the same as that from higher concentrations of isoprene (see Supporting Information).

Measurements of aerosol growth and SOA yield over a range of isoprene concentrations were not carried out for

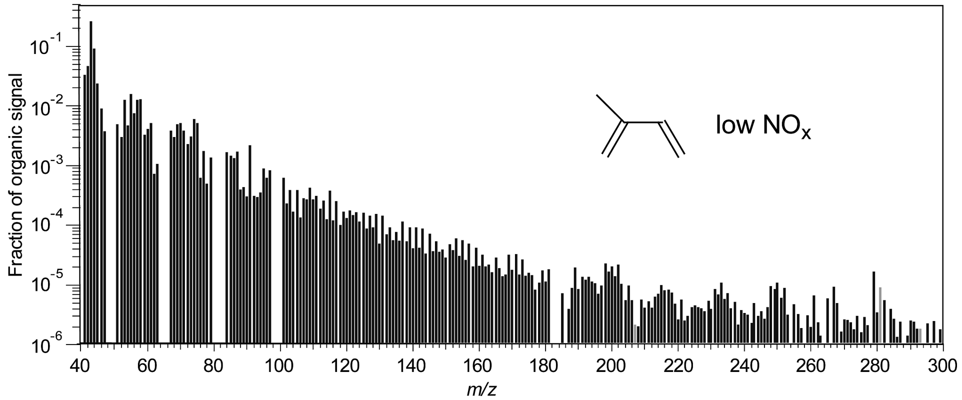

FIGURE 3. Typical AMS spectrum (*m/z* ≥ 40) of SOA formed from isoprene photooxidation under low-NO_x conditions. For clarity, masses in which the organics overlap with peaks from sulfate (*m/z* 48−50, 64−66, 80−83, 98−100) and tungsten (from the filament; *m/z* 182, 184−186) have been omitted. Light gray bars correspond to negative values after data analysis.

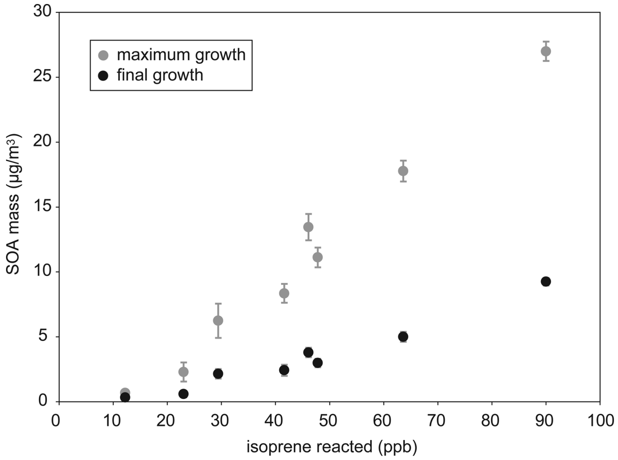

FIGURE 4. Measured SOA growth versus isoprene reacted (low-NO_x conditions). Gray circles: maximum growth; black circles: final growth, after photochemical loss of SOA (see text for details). Each pair of points (at a single value of isoprene reacted) corresponds to one experiment. Data are taken from Table 1; SOA mass is calculated using a density of 1.25 g/cm³.

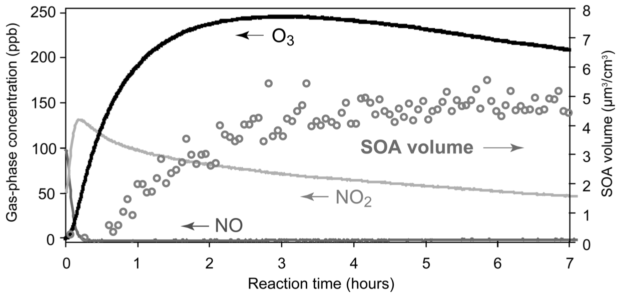

FIGURE 5. Reaction profile of a typical isoprene photooxidation experiment under high-NO_x conditions (Experiment 11). Decay of isoprene is rapid, with most consumed in the first 30 min of reaction, so it is omitted for clarity.

the high-NO_x case because we have presented such results previously (*24*). Instead, we focus on the dependence of SOA growth on NO_x concentration, in which initial isoprene concentrations are held essentially constant (45 ± 4 ppb). Shown in Table 2 are experimental conditions and results for the high-NO_x experiments. Ammonium sulfate seed is used in all cases to provide surface area onto which semivolatile products may condense. Running the reaction in the absence of seed leads to the formation of large number concentrations (50 000−150 000 particles/cm³) of very small particles, due to the fast rate of formation of condensable products. Such small particles are lost to the walls very quickly, precluding accurate (wall-loss-corrected) volume measurements, so seed particles are necessary. Under high-NO_x conditions, SOA density is determined to be 1.35 (±0.05) g/cm³. Shown in Figure 7 is SOA growth versus initial NO_x concentration. The SOA yields measured in these experiments are somewhat higher than those reported in our previous study (*24*); this may be a result of differences in gas-phase chemistry (such as initial [NO_x], rate of change of [NO_x], and the [NO]:[NO_2] ratio), photolytic conditions, and/or RH. Understanding these possible effects requires further study. We note that in one previous photooxidation study (*33*), no RH-dependence of SOA yields was observed.

Isoprene Oxidation Products. Two additional studies are carried out in which methacrolein (500 ppb, Aldrich, 95%) and methyl vinyl ketone (500 ppb, Aldrich, 99%) are photooxidized under high-NO_x conditions (initial [NO_x] = 860 ppb). While the oxidation of methyl vinyl ketone produces no SOA, methacrolein oxidation produces substantial SOA (170 ± 1 μm³/cm³), as reported previously in an experiment using HONO as the radical precursor (*24*). The AMS spectrum of SOA from methacrolein oxidation is shown in Figure 8.

Discussion

General Mechanism of SOA Growth. In both the low- and high-NO_x experiments, SOA growth does not begin until a significant fraction (>50%) of the isoprene is consumed, and SOA growth continues even after the isoprene is fully consumed. This implies the existence of a rate-limiting step in SOA formation following the initial OH-isoprene reaction. As discussed in previous work (*24*), this step is likely the oxidation of first-generation reaction products; both double bonds of isoprene must be oxidized, resulting in the addition of up to four polar functional groups to the carbon skeleton. This conclusion is strongly supported by the observation of SOA production from the oxidation of methacrolein, a major first-generation isoprene oxidation product. The role of second-generation products in SOA formation (from the oxidation of isoprene and other biogenic hydrocarbons) is discussed in detail by Ng et al. (*34*).

Shown in Figure 9 is the simplified mechanism of the initial steps of the OH + isoprene reaction, leading to the formation of first-generation molecular products. The hydroxyl radical adds to one of the double bonds, primarily at the 1- or 4-position, and the subsequent addition of O_2 leads to the formation of six possible isoprene hydroxperoxy radicals (for simplicity, only one is shown in Figure 9). The fate of this radical depends on the level of ambient NO_x. At high NO_x ([NO] ≫ [HO_2] + [RO_2]), peroxy radicals primarily react with NO. They may also react with NO_2 to form peroxynitrates (RO_2NO_2), but these are thermally unstable, with lifetimes shorter than 1s, so they are generally unimportant under most conditions. Isoprene hydroxyperoxy radicals plus NO forms either hydroxynitrates or hydroxyalkoxy radicals, the latter of which undergo decomposition, isomerization, or hydrogen abstraction by O_2 to form methacrolein, methyl vinyl ketone, and other first-generation isoprene oxidation products shown in Figure 1.

The rates and products of the oxidation reactions of many of these first-generation products are poorly constrained. The oxidation reactions of methacrolein and methyl vinyl ketone are well-studied, with known products accounting for >90% of the total reaction (*35*−*37*). Based on our observation of SOA production from methacrolein oxidation, it is clear that some products of the OH-methacrolein reaction (possibly minor, previously undetected species) are condensable. The similarity between the mass spectrum of SOA from methacrolein oxidation (Figure 8) and that of isoprene oxidation (Figure 6) strongly suggests that methacrolein is a principal intermediate in SOA formation from isoprene photooxidation under high-NO_x conditions. It is not straightforward to quantify the contribution of methacrolein oxidation products to SOA from isoprene oxidation, due to the dependence of gas-particle partitioning on available organic particulate matter (*31*, *34*). Products of the oxidation of other first-generation products, accounting for 20−40% of the OH + isoprene reaction, have, for the most part, not been measured, but may also play a role in SOA formation.

The oxidation of isoprene under low-NO_x conditions has received far less study and so is more uncertain. When concentrations of peroxy radicals (HO_2 and RO_2) approach the concentration of NO, RO_2 + HO_2 and RO_2 + RO_2 reactions become competitive with RO_2 + NO, and a different product distribution is expected (lower half of Figure 9). The reaction of isoprene hydroxyperoxy radicals with other RO_2 radicals is expected to lead to a mixture of hydroxycarbonyls, diols, and products from alkoxy radical reactions, such as methacrolein and methyl vinyl ketone, all of which have been

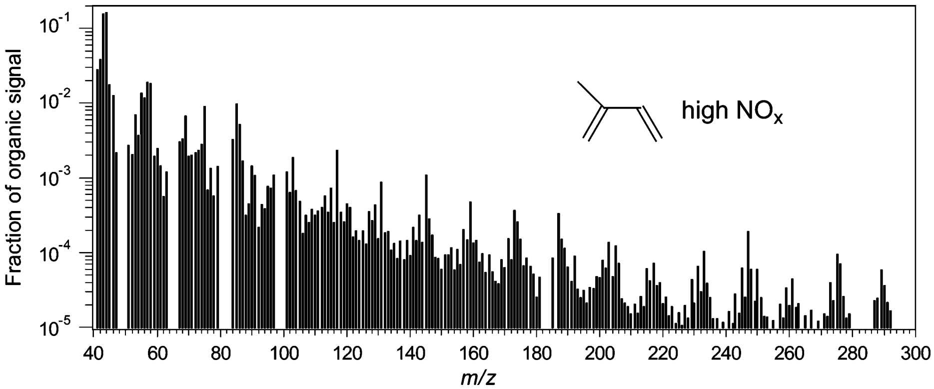

FIGURE 6. Typical AMS spectrum of SOA formed from isoprene photooxidation under high-NO_x conditions. See description of Figure 3 for details.

TABLE 2. Experimental Conditions and Results for High-NO_x Experiments[a]

expt. no.	isoprene reacted (ppb)	initial [NO] (ppb)	Initial [NO_x] (ppb)	$(NH_4)_2SO_4$ volume ($\mu m^3/cm^3$)	maximum [O_3] (ppb)	ΔM_o ($\mu g/m^3$)[b]	SOA yield (%)	T_{max} (°C)
9	46.7	242	266	4.6 ± 0.2	342	6.3 ± 1.0	4.7 ± 0.7	28.3
10	43.5	496	526	7.1 ± 0.3	389	2.9 ± 1.2	2.3 ± 0.9	28.3
11	42.7	98	129	6.4 ± 0.7	245	6.7 ± 1.3	5.5 ± 1.0	28.1
12	49.1	51	78	6.5 ± 0.3	256	5.6 ± 1.3	4.0 ± 0.9	28.2
13	42.7	337	405	4.8 ± 0.2	508	4.6 ± 1.0	3.8 ± 0.8	28.3
14	42.0	708	745	4.7 ± 0.3	492	1.7 ± 1.1	1.4 ± 0.9	27.5

[a] Stated uncertainties (2σ) are from scatter in particle volume measurements. [b] Assuming an SOA density of 1.35 g/cm^3.

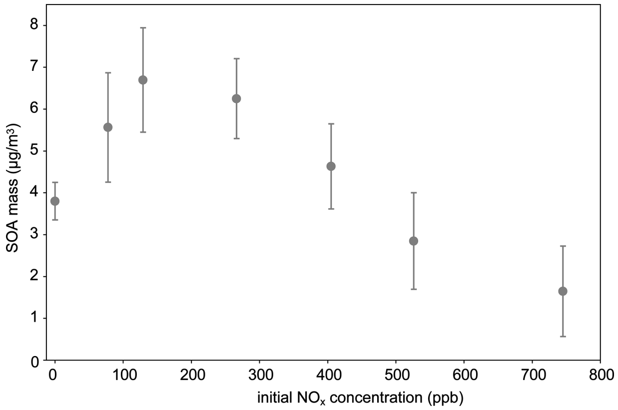

FIGURE 7. SOA growth as a function of initial NO_x concentration, for a fixed isoprene concentration (45 ± 4 ppb). Results shown are from Table 2; the NO_x-free point is final growth from Experiment 2, Table 1.

detected in the laboratory (*7*, *38–40*); yields and carbon balance are not fully established. The hydroxyhydroperoxides expected from the reaction of HO_2 with isoprene RO_2 radicals have not been conclusively identified in the laboratory, though they have been tentatively identified in the troposphere (*41*). Miyoshi et al. (*7*) found that under conditions in which the $HO_2 + RO_2$ reaction dominates, organic hydroperoxides are formed in high concentrations with no other identifiable gas-phase products. The further reactions of these oxidation products have not been studied. In particular, the tropospheric fate of isoprene hydroxyhydroperoxides is highly uncertain, and the relative importance of photolysis and reaction with OH is largely unknown, as is the product distribution from each channel.

In summary, the lack of experimental data on the second-generation products (and, at low NO_x, even the first generation products) of isoprene oxidation makes it difficult to know the exact chemical mechanism of SOA formation. Under high-NO_x conditions, methacrolein is certainly an important intermediate in the production of SOA. Numerous pathways may be put forth which lead to the formation of relatively nonvolatile second-generation oxidation products, with 4–5 carbon atoms and 3–4 polar functional (carbonyl, hydroxy, hydroperoxy, nitrate, or acid) groups. Further studies of the gas- and particle-phase products of isoprene oxidation would be useful for identifying the detailed chemistry of SOA formation.

In addition, particle-phase reactions of these products are likely to contribute to SOA formation. From the aerosol mass spectra (Figures 3, 6, and 8), it is clear that oligomers are formed. At both high- and low-NO_x, a significant fraction of the organic mass is from fragments of high molecular weight ($m/z > 200$), corresponding to species with more than five carbon atoms (C5 products will have masses ≤226, the mass of the dihydroxy-dinitrate). An important role of such reactions in SOA formation may explain why methacrolein oxidation forms SOA but methyl vinyl ketone oxidation does not, as aldehydes are substantially more susceptible to nucleophilic attack (and hence oligomerization reactions) than are ketones (*42*). The chemical composition of the SOA will be discussed in detail in a forthcoming publication.

Role of NO_x. Despite uncertainties in the detailed chemical mechanism of isoprene oxidation, the dependence of SOA growth on NO_x level (Figure 7) provides some insight into the underlying chemistry of SOA formation. At high NO_x (>200 ppb), SOA yield is found to decrease with increasing NO_x; similar decreases have been observed in a number of SOA yield measurements (*12*, *43–49*). This dependence has been attributed to two effects: (1) relative levels of different oxidants (OH, NO_3, and O_3) present in the reaction system (*45*), and (2) the chemistry of peroxy radicals (*43*, *46*, *49*). In the present study, OH is the dominant oxidant throughout the course of the experiment, due to the continual production of OH radicals from H_2O_2 photolysis. The O_3 and NO_3 produced in the high-NO_x experiments account for a negligible fraction of the isoprene reacted, because they are only formed once NO concentration is near zero, typically

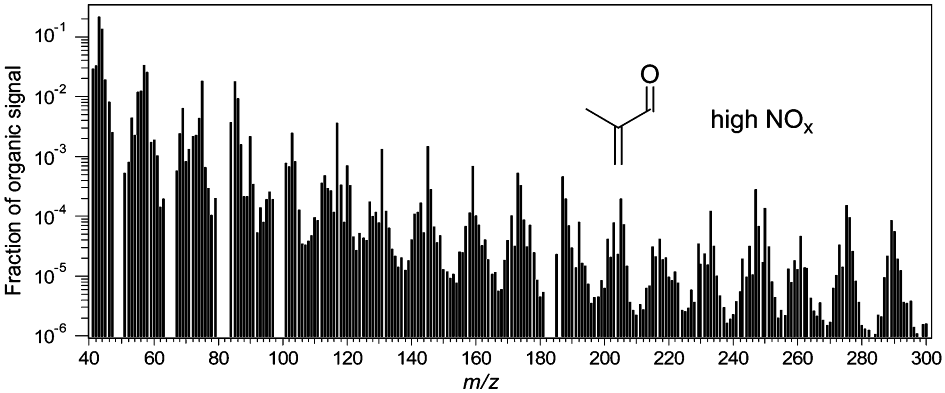

FIGURE 8. AMS spectrum of SOA formed from methacrolein photooxidation under high-NO_x conditions. See description of Figure 3 for details. The spectrum shown is similar to that of isoprene photooxidation (Figure 6), with the same major peaks, suggesting the importance of methacrolein as an intermediate in SOA formation from isoprene oxidation under high-NO_x conditions.

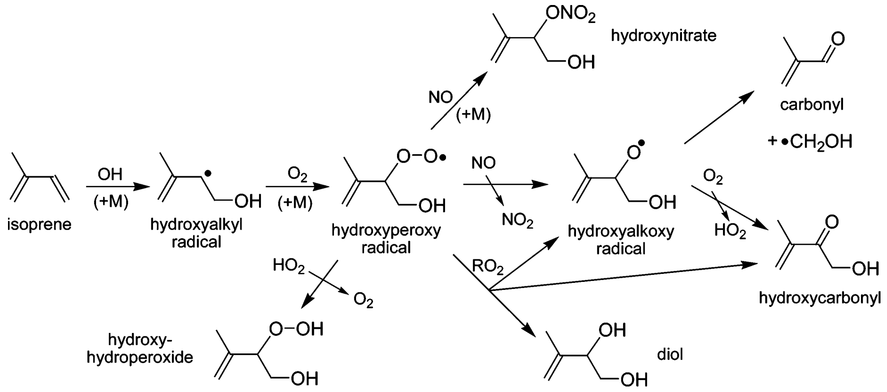

FIGURE 9. Reaction mechanism of isoprene oxidation, showing the formation of first-generation products. For clarity, only one of four possible alkyl radicals and one of six possible hydroperoxy radicals are shown. The first-generation reaction products are all unsaturated so they may be rapidly oxidized to second-generation products.

after all isoprene has been reacted away. Isoprene oxidation products may react with O_3 or NO_3, but for major oxidation products, such reactions are slow (*29*) and are expected to be unimportant. There may, however, be exceptions (for example, 3-methyl-furan reacts rapidly with NO_3 (*50*)), and we cannot rule out the possibility that reactions of O_3 or NO_3 may be sinks for minor isoprene oxidation products.

Nonetheless, all of the oxidation of isoprene, and the oxidation of most of its reaction products, is initiated by the OH radical; the observed NO_x dependence of SOA yields is likely a result not of differences in OH, O_3, and NO_3 reactions, but of rather differences in peroxy radical chemistry. In the present experiments, organic peroxy radicals will react with either HO_2 (formed in the OH + H_2O_2 reaction) or NO. RO_2 + RO_2 reactions are relatively unimportant because the concentration of H_2O_2 (which reacts with OH to form HO_2) is much higher than that of isoprene (which reacts with OH to form RO_2), and HO_2 + RO_2 reactions are significantly faster than RO_2 self-reactions (*51*). As mentioned above, peroxynitrate formed from RO_2 + NO_2 serves as only as a short-lived reservoir of RO_2. Thus the fate of RO_2 radicals depends on the relative concentrations of HO_2 and NO. At high [NO], alkoxy radicals and organic nitrates will be formed from the RO_2 + NO reaction; small alkoxy radicals are expected to fragment, and organic nitrates may be relatively volatile (*49*). On the other hand, at low [NO], RO_2 + HO_2 reactions form hydroperoxides, recently shown in both experimental (*52*) and modeling (*46, 53, 54*) studies to be important components of SOA. High concentrations of NO, therefore, appear to suppress the formation of SOA by suppressing hydroperoxide formation, consistent with the conclusions of other studies of the NO_x-dependence of SOA formation (*43*, *46*, *49*). This also explains our observations that SOA growth begins only when NO concentrations approach zero, which appears to be a general feature of chamber measurements of SOA formation from hydrocarbon photooxidation (e.g., *45*–*47*, *54*). As discussed previously (*24*), in the studies of Pandis et al. (*12*) and Edney et al. (*13*), [NO] did not fall below ~30 ppb, and no SOA was produced. Thus the formation of hydroxy-hydroperoxides is likely to play an important role in SOA formation from isoprene photooxidation. This is consistent with the results of Miyoshi et al. (*7*), who report the formation of both gas-phase hydroperoxides and particles from the OH + isoprene reaction at low NO_x and high HO_2. In the particle phase, hydroperoxides may react further, oxidizing organics or reacting with aldehydes to form peroxyhemiacetals (*55*), oligomeric species which may account for some of the high-MW peaks seen in AMS spectra of SOA (Figure 6).

However, the suppression of SOA formation by NO does not fully explain the observed NO_x-dependence of aerosol yields from isoprene photooxidation, as yields increase with NO_x at low NO concentrations (Figure 7). Similar NO_x-dependences of aerosol yield have been observed in the photooxidation of α- and β-pinene (*12*, *44*); however, those experiments were carried out under very different oxidative conditions than in the present study and so may not be directly comparable. The increase in SOA growth with NO_x may be the result of changes in reaction conditions over the course of the experiments; over time the [NO]/[HO_2] ratio decreases (as NO is converted to NO_2, and the suppression of HO_2 by NO decreases), which may lead to a switch from high-NO_x to low-NO_x conditions. This could lead to a complex dependence of SOA formation on NO_x; peroxy radicals formed in the first oxidation step (OH + isoprene) react with NO, whereas peroxy radicals formed by the oxidation of isoprene reaction products react with HO_2. Such a change in NO_x conditions may be relevant in the troposphere during transport from a polluted to an unpolluted region, but it would be preferable to measure SOA yields under conditions in which the [NO]/[HO_2] ratio, and thus the fate of organic peroxy radicals, stays constant over the course of the entire experiment. More generally, to apply chamber results to atmospheric conditions, it is important that the [NO]/[HO_2] ratio be well-constrained; in our experiments, SOA is suppressed by 100s of ppb of NO, though in the atmosphere this is likely to occur at lower NO concentrations due to elevated HO_2 concentrations (estimated at 100s of ppt) in the chamber. Thus, reaction conditions need to be better controlled and characterized before parameterizations of SOA yields as a function of [NO_x] may be obtained.

It should be noted that the NO_x-dependence of SOA growth measured in this work may not apply generally to all SOA-forming reactions. For example, Edney et al. (*13*) showed that, in the presence of SO_2, isoprene oxidation forms SOA even in the presence of NO, suggesting that enhanced reactive uptake by acidic aerosol particles may counteract the reduced production of condensable species at high NO_x. Additionally, the reaction of NO with large peroxy radicals will form alkoxy radicals which isomerize rather than fragment. These will form large, multifunctional products, which may efficiently partition into the aerosol phase. Thus hydrocarbons substantially larger than isoprene are expected to form SOA even under high-NO_x conditions. Indeed, recently SOA formation from the OH-initiated oxidation of long-chain alkanes has been observed in the presence of several ppm of NO (*56*). In such cases, SOA yields may even be higher at high NO_x. Thus SOA formation may be a complex function of NO_x level, and future study is required.

Rapid Photochemical Loss of SOA. As noted earlier, under low-NO_x conditions ([NO_x] < 1 ppb), initial SOA growth from isoprene oxidation is large (sometimes reaching yields of >10%), but is followed by a rapid decrease in aerosol volume as the reaction progresses (Figure 2). To our knowledge such an effect has not been reported in previous chamber studies of SOA formation. The decrease in SOA, characterized by a shrinking of particles rather than a reduction in particle number, is a photochemical effect, as it occurs only during chamber irradiation (when UV photons and OH radicals are present), ceasing immediately when the chamber lights are turned off. Therefore, this may be an example of photochemical "aging", or oxidative processing, of the SOA. We do not observe rapid loss of SOA formed in the low-NO_x photooxidation of β-pinene (140 ppb), indicating that it is not a general feature of the irradiation of all hydrocarbon/H_2O_2 mixtures.

The photochemical mechanism of volatilization is not clear at present. Recent experimental evidence shows that the reaction of gas-phase OH radicals with condensed organics may lead to efficient volatilization of organic compounds, thereby serving as a sink for SOA in the troposphere (*57*). However, such a mechanism probably cannot account for the fast rate of SOA loss observed, and we observe no obvious dependence of the rate of SOA loss on surface area, which would be expected for reactions of gas-phase oxidants with condensed-phase organics.

Instead, the SOA loss may be a result of gas-phase or particle-phase oxidation reactions continuing after particle formation. Once semivolatile compounds reach gas-particle equilibrium, any further gas-phase losses (by reaction with OH or photolysis) of those compounds may drive equilibrium away from the particle phase, leading to a decrease in SOA mass. If all losses are from such gas-phase reactions, and these reactions (rather than gas-particle partitioning) are the rate-limiting step, then the SOA loss (0.006−0.018 min^{-1}) is consistent with the reaction with OH ($k_{OH} = 4.0 \times 10^{-11}$-$1.2 \times 10^{-10}$ $cm^3\ molec^{-1}\ s^{-1}$ for $[OH] = 2.5 \times 10^6/cm^3$), photolysis ($J = 0.006-0.018\ min^{-1}$), or some combination of the two. Given that this effect is seen only at low NO_x, these reactive compounds are likely to be organic hydroperoxides. If loss is by photolysis, the inferred *J* value is significantly larger (by 1 or 2 orders of magnitude) than that of the simplest organic peroxide, CH_3OOH (*29*). The efficient photolysis of organic hydroperoxides has been put forth as an explanation for discrepancies between measured tropospheric ozone production and modeled HO_x chemistry (*58*), as well as for the observation that SOA yields from α-pinene ozonolysis are lower under UV irradiation than under dark conditions (*59*). In the latter case, the underlying chemistry (and inferred photolytic lifetime) is substantially different than in the present study, but it is clear that the photochemistry of structurally complex organic peroxides deserves further study.

However, gas-phase reaction is unlikely to account for all of the observed loss, as AMS results show that the chemical composition of the SOA changes over the course of the decrease; a number of high-MW organic fragments are observed to increase in intensity even during the rapid loss of organic aerosol mass. This may be a result of particle-phase reactions, such as the photolysis of condensed-phase hydroperoxides. Such reactions would form OH and alkoxy radicals within the aerosol, which would serve to rapidly oxidize other SOA components; products of such reactions may be quite volatile, leading to the loss of SOA mass, or oligomeric and highly nonvolatile. In a forthcoming publication, in which we focus on the chemical composition of SOA from isoprene oxidation, the chemistry of this photochemical aging process will be explored in greater detail.

Acknowledgments

This research was funded by the U.S. Environmental Protection Agency Science to Achieve Results (STAR) Program grant number RD-83107501-0, managed by EPA's Office of Research and Development (ORD), National Center for Environmental Research (NCER), and by the U.S. Department of Energy Biological and Environmental Research Program DE-FG03-01ER63099; this work has not been subjected to the EPA's required peer and policy review and, therefore, does not necessarily reflect the views of the Agency and no official endorsement should be inferred.

Supporting Information Available

Details of the blank runs, tests for the role of impurities, and low-concentration runs. This material is available free of charge via the Internet at http://pubs.acs.org.

Literature Cited

(1) Kanakidou, M.; et al. Organic aerosol and global climate modelling: a review. *Atmos. Chem. Phys.* **2005**, *5*, 1053−1123.

(2) Chung, S. H.; Seinfeld, J. H. Global distribution and climate forcing of carbonaceous aerosols. *J. Geophys. Res.* **2002**, *107*, 4407, doi10.1029/2001JD001397.

(3) Tsigaridis, K.; Kanakidou, M. Global modelling of secondary organic aerosol in the troposphere: a sensitivity analysis. *Atmos. Chem. Phys.* **2003**, *3*, 1849−1869.

(4) Guenther, A.; et al. A global model of natural volatile organic compound emissions. *J. Geophys. Res.* **1995**, *100*, 8873−8892.

(5) Tuazon, E. C.; Atkinson, R. Product study of the gas-phase reaction of isoprene with the OH radical in the presence of NO_x. *Int. J. Chem. Kinet.* **1990**, *22*, 1221−1236.

(6) Paulson, S. E.; Flagan, R. C.; Seinfeld, J. H. Atmospheric photooxidation of isoprene, Part I: The hydroxyl radical and ground-state atomic oxygen reactions. *Int. J. Chem. Kinet.* **1992**, *24*, 79−101.

(7) Miyoshi, A.; Hatakeyama, S.; Washida, N. OH radical-initiated photooxidation of isoprene: An estimate of global CO production. *J. Geophys. Res.* **1994**, *99*, 18,779−18,787.

(8) Sprengnether, M.; Demerjian, K. L.; Donahue, N. M.; Anderson, J. G. Product analysis of the OH oxidation of isoprene and 1,3-butadiene. *J. Geophys. Res.* **2002**, *107*, D15, 4268, doi: 10.1029/2001JD000716.

(9) Chen, X.; Hulbert, D.; Shepson, P. B. Measurement of the organic nitrate yield from OH reaction with isoprene. *J. Geophys. Res.* **1998**, *103*, 25,563−25,568.

(10) Zhao, J.; Zhang, R.; Fortner, E. C.; North, S. W. Quantification of hydroxycarbonyls from OH-isoprene reactions. *J. Am. Chem. Soc.* **2004**, *126*, 2686−2687.

(11) Baker, J.; Arey, J.; Atkinson, R. Formation and reaction of hydroxycarbonyls from the reaction of OH radicals with 1,3-butadiene and isoprene. *Environ. Sci. Technol.* **2005**, *39*, 4091−4099.

(12) Pandis, S. N.; Paulson, S. E.; Seinfeld, J. H.; Flagan, R. C. Aerosol formation in the photooxidation of isoprene and β-pinene, *Atmos. Environ.* **1991** *25A*, 997−1008.

(13) Edney, E. O.; Kleindienst, T. E.; Jaoui, M.; Lewandowski, M.; Offenberg, J. H.; Wang, W.; Claeys, M. Formation of 2-methyl tetrols and 2-methylglyceric acid in secondary organic aerosol from laboratory irradiated isoprene/NO_x/SO_2/air mixtures and their detection in ambient $PM_{2.5}$ samples collected in the eastern United States. *Atmos. Environ.* **2005**, *39*, 5281−5289.

(14) Claeys, M.; et al. Formation of secondary organic aerosol through photooxidation of isoprene. *Science* **2004**, *303*, 1173−1176.

(15) Ion, A. C.; Vermeylen, R.; Kourtchev, I.; Cafmeyer, J.; Chi, X.; Gelencsér. A.; Maenhaut, W.; Claeys, M. Polar organic compounds in rural $PM_{2.5}$ aerosols from K-puszta, Hungary, during a 2003 summer field campaign: sources and diel variations. *Atmos. Chem. Phys.* **2005**, *5*, 1805−1814.

(16) Kourtchev, I.; Ruuskanen, T.; Maenhaut, W.; Kulmala, M.; Claeys, M. Observation of 2-methyltetrols and related photo-oxidation products of isoprene in boreal forest aerosols from Hyytiälä, Finland. *Atmos. Chem. Phys.* **2005**, *5*, 2761−2770.

(17) Claeys, M.; Wang, W.; Ion, A. C.; Kourtchev, I.; Gelencsér, A.; Maenhaut, W. Formation of secondary organic aerosols from isoprene and gas-phase oxidation products through reaction with hydrogen peroxide. *Atmos. Environ.* **2004**, *38*, 4093−4098.

(18) Limbeck, A.; Kulmala, M.; Puxbaum, H. Secondary organic aerosol formation in the atmosphere via heterogeneous reaction of gaseous isoprene on acidic particles. *Geophys. Res. Lett.* **2003**, *30*, 1996−1999.

(19) Czoschke, N. M.; Jang, M.; Kamens, R. M. Effect of acidic seed on biogenic secondary organic aerosol growth. *Atmos. Environ.* **2003**, *37*, 4287−4299.

(20) Matsunaga, S.; Mochida, M.; Kawamura, K. Growth of organic aerosols by biogenic semi-volatile carbonyls in the forestal atmosphere. *Atmos. Environ.* **2003**, *37*, 2045−2050.

(21) Matsunaga, S.; Mochida, M.; Kawamura, K. Variation on the atmospheric concentrations of biogenic compounds and their removal processes in the northern forest at Moshiri, Hokkaido Island in Japan. *J. Geophys. Res.* **2004**, *109*, D04302, doi: 10.1029/2003JD004100.

(22) Ervens, B.; Feingold, G.; Frost, G. J.; Kreidenweis, S. M. A modeling study of aqueous production of dicarboxylic acids: 1. Chemical pathways and speciated organic mass production. *J. Geophys. Res.* **2003**, *109*, D15205, doi: 10.1029/2003JD004387.

(23) Lim, H.-J.; Carlton, A. G.; Turpin, B. J. Isoprene forms secondary organic aerosol through cloud processing: model simulations, *Environ. Sci. Technol.* **2005**, *39*, 4441−4446.

(24) Kroll, J. H.; Ng, N. L.; Murphy, S. M.; Flagan, R. C.; Seinfeld, J. H. Secondary organic aerosol formation from isoprene photooxidation under high-NO_x conditions. *Geophys. Res. Lett.* **2005**, *32*, L18808, doi: 10.1029/2005GL023637.

(25) Cocker, D. R., III; Flagan, R. C.; Seinfeld, J. H. State-of-the-art chamber facility for studying atmospheric aerosol chemistry. *Environ. Sci. Technol.* **2001**, *35*, 2594−2601.

(26) Keywood, M. D.; Varutbangkul, V.; Bahreini, R.; Flagan, R. C.; Seinfeld, J. H. Secondary organic aerosol formation from the ozonolysis of cycloalkenes and related compounds. *Environ. Sci. Technol.* **2004**, *38*, 4157−4164.

(27) Drewnick F.; et al. A new time-of-flight aerosol mass spectrometer (TOF-AMS)—Instrument description and first field deployment. *Aerosol Sci. Technol.* **2005**, *39*, 637−658.

(28) Atkinson, R.; et al. Evaluated kinetic and photochemical data for atmospheric chemistry: volume 1 − gas-phase reactions of O_x, HO_x, NO_x, and SO_x species. *Atmos. Chem. Phys.* **2004**, *4*, 1461−1738.

(29) Atkinson, R.; et al. Evaluated kinetic and photochemical data for atmospheric chemistry: Supplement VII, Organic species, *J. Phys. Chem. Ref. Data* **1999**, *28*, 191−393.

(30) Bahreini, R.; Keywood, M. D.; Ng, N. L.; Varutbangkul, V.; Gao, S.; Flagan, R. C.; Seinfeld, J. H. Measurements of secondary organic aerosol (SOA) from oxidation of cycloalkenes, terpenes, and *m*-xylene using an Aerodyne aerosol mass spectrometer. *Environ. Sci. Technol.* **2005**, *39*, 5674−5688.

(31) Odum, J. R.; Hoffmann, T.; Bowman, F.; Collins, D.; Flagan, R. C.; Seinfeld, J. H. Gas/particle partitioning and secondary organic aerosol yields. *Environ. Sci. Technol.* **1996**, *30*, 2580−2585.

(32) Kroll, J. H.; Seinfeld, J. H. Representation of secondary organic aerosol (SOA) laboratory chamber data or the interpretation of mechanisms of particle growth. *Environ. Sci. Technol.* **2005**, *39*, 4159−4165.

(33) Cocker, D. R., III; Mader, B. T.; Kalberer, M.; Flagan, R. C.; Seinfeld, J. H. The effect of water on gas-particle partitioning of secondary organic aerosol: II. *m*-xylene and 1,3,5-trimethylbenzene photooxidation systems. *Atmos. Environ.* **2001**, *35*, 6073−6085.

(34) Ng, N. L.; Kroll, J. H.; Keywood, M. D.; Bahreini, R.; Varutbangkul, V.; Flagan, R. C.; Seinfeld, J. H.; Lee, A.; Goldstein, A. H. Contribution of first- versus second-generation prducts to secondary organic aerosols formed in the oxidation of biogenic hydrocarbons. *Environ. Sci. Technol.* **2006**, in press.

(35) Tuazon, E. C.; Atkinson, R. A product study of the gas-phase reaction of methyl vinyl ketone with the OH radical in the presence of NO_x. *Int. J. Chem. Kinet.* **1989**, *21*, 1141−1152.

(36) Tuazon, E. C.; Atkinson, R. A product study of the gas-phase reaction of methacrolein with the OH radical in the presence of NO_x. *Int. J. Chem. Kinet.* **1990**, *22*, 591−602.

(37) Orlando, J. J.; Tyndall, G. S.; Paulson, S. E. Mechanism of the OH-initiated oxidation of methacrolein. *Geophys. Res. Lett.* **1999**, *26*, 2191−2194.

(38) Ruppert, L.; Becker, K. H. A product study of the OH radical-initiated oxidation of isoprene: formation of C_5-unsaturated diols. *Atmos. Environ.* **2000**, *34*, 1529−1542.

(39) Benkelberg, H.-J.; Böge, O.; Seuwen, R.; Warneck, P. Product distributions fro the OH radical-induced oxidation of but-1-ene, methyl-substituted but-1-enes and isoprene in NO_x-free air. *Phys. Chem. Chem. Phys.* **2000**, *2*, 4029−4039.

(40) Lee, W.; Baasandorj, M.; Stevens, P. S.; Hites, R. A. Monitoring OH-initiated oxidation kinetics of isoprene and its products using online mass spectrometry. *Environ. Sci. Technol.* **2005**, *39*, 1030−1036.

(41) Warneke, C.; et al. Isoprene and its oxidation products methyl vinyl ketone, methacrolein, and isoprene related peroxides measured online over the tropical rain forest of Surinam in March 1998. *J. Atmos. Chem.* **2001**, *38*, 167−185.

(42) McMurry, J. *Organic Chemistry,* 4th ed.; Brooks/Cole: Pacific Grove, CA, 1995.

(43) Hatakeyama, S.; Izumi, K.; Fukuyama, T.; Akimoto, H.; Washida, N. Reactions of OH with α-pinene and β-pinene in air: estimates of global CO production from the atmospheric oxidation of terpenes. *J. Geophys. Res.* **1991**, *96*, D1, 947−958.

(44) Zhang, S.-H.; Shaw, M.; Seinfeld, J. H.; Flagan, R. C. Photochemical aerosol formation from α-pinene and β-pinene. *J. Geophys. Res.* **1992**, *92*, D18, 20, 717−720, 729.

(45) Hurley, M. D.; Sokolov, O.; Wallington, T. J.; Takekawa H.; Karasawa M.; Klotz B.; Barnes I.; Becker, K. H. Organic aerosol formation during the atmospheric degradation of toluene. *Environ. Sci. Technol.* **2001**, *35*, 1358−1366.

(46) Johnson, D.; Jenkin, M. E.; Wirtz, K.; Martín-Reviejo, M. Simulating the formation of secondary organic aerosol from the photooxidation of toluene. *Environ. Chem.* **2004**, *1*, 150−165.

(47) Martin-Revíejo, M.; Wirtz, K. Is benzene a precursor for secondary organic aerosol? *Environ. Sci. Technol.* **2005**, *39*, 1045−1054.

(48) Song, C.; Na, K.; Cocker, D. R., III Impact of the hydrocarbon to NO_x ratio on secondary organic aerosol formation. *Environ. Sci. Technol.* **2005**, *39*, 3143−3149.

(49) Presto, A. A.; Huff Hartz, K. E.; Donahue, N. M. Secondary organic aerosol production from ozonolysis: 2. Effect of NO_x concentration. *Environ. Sci. Technol.* **2005**, *39*, 7046.

(50) Alvarado, A.; Atkinson, R.; Arey, J. Kinetics of the gas-phase reactions of NO_3 radicals and O_3 with 3-methylfuran and the OH radical yield from the O_3 reaction. *Int. J. Chem. Kinet.* **1996**, *28*, 905−909.

(51) Jenkin, M. E.; Boyd, A. A.; Lesclaux, R. Peroxy radical kinetics resulting from the OH-initiated oxidation of *1*,*3*-butadiene, *2*,*3*-dimethyl-*1*,*3*-butadiene and isoprene. *J. Atmos. Chem.* **1998**, *29*, 267−298.

(52) Docherty, K. S.; Wu, W.; Lim, Y. B.; Ziemann, P. J. Contributions of organic peroxides to secondary organic aerosol formed from reactions of monoterpenes with O_3. *Environ. Sci. Technol.* **2005**, *39*, 4049−4059.

(53) Bonn, B.; von Kuhlmann, R.; Lawrence, M. G. High contribution of biogenic hydroperoxides to secondary organic aerosol formation. *Geophys. Res. Lett.* **2004**, *31*, L10108, doi: 10.1029/2003GL019172.

(54) Johnson, D.; Jenkin, M. E.; Wirtz, K.; Martín-Reviejo, M. Simulating the formation of secondary organic aerosol from the photooxidation of aromatic hydrocarbons. *Environ. Chem.* **2005**, *2*, 35−48.

(55) Tobias, H. J.; Ziemann, P. J. Thermal desorption mass spectrometric analysis of organic aerosol formed from reactions of 1-tetradecene and O_3 in the presence of alcohols and carboxylic acids. *Environ. Sci. Technol.* **2000**, *34*, 2105−2115.

(56) Lim, Y. B.; Ziemann, P. J. Products and mechanism of secondary organic aerosol formation from reactions of *n*-alkanes with OH radicals in the presence of NO_x. *Environ. Sci. Technol.* **2005**, *39*, 9229−9236.

(57) Molina, M. J.; Ivanov, A. V.; Trakhtenberg, S.; Molina, L. T. Atmospheric evolution of organic aerosol. *Geophys. Res. Lett.* **2004**, *31*, L22104, doi: 10.1029/2004GL020910.

(58) Thornton, J. A.; et al. Ozone production rates as a function of NO_x abundances and HO_x production rates in the Nashville urban plume. *J. Geophys. Res.* **2002**, *107*, D12, doi: 10.1029/2001JD000932.

(59) Presto, A. A.; Huff Hartz, K. E.; Donahue, N. M. Secondary organic aerosol production from terpene ozonolysis. 1. Effect of UV radiation. *Environ. Sci. Technol.* **2005**, *39*, 7036−7045.

Received for review December 3, 2005. Revised manuscript received January 13, 2006. Accepted January 18, 2006.

ES0524301

Appendix B

Apportionment of Primary and Secondary Organic Aerosols in Southern California during the 2005 Study of Organic Aerosols in Riverside (SOAR-1)*

---

*This chapter is reproduced by permission from. "Apportionment of primary and secondary organic aerosols in Southern California during the 2005 study of organic aerosols in Riverside (SOAR-1)." K.S. Docherty, E. A. Stone, I. M. Ulbrich, P. F. DeCarlo, D. C. Snyder, J. J. Schauer, R. E. Peltier, R. J. Weber, S. M. Murphy, J. H. Seinfeld, B. D. Grover, D. J. Eatough, J. L. Jiimenez, *Environmental Science and Technology,* 42 (20), 7655-7662, 2008. Copyright 2008. American Chemical Society.

Environ. Sci. Technol. **2008,** *42,* 7655–7662

Apportionment of Primary and Secondary Organic Aerosols in Southern California during the 2005 Study of Organic Aerosols in Riverside (SOAR-1)

KENNETH S. DOCHERTY,[†,‡]
ELIZABETH A. STONE,[∥]
INGRID M. ULBRICH,[†,‡]
PETER F. DeCARLO,[†,§,○]
DAVID C. SNYDER,[∥] JAMES J. SCHAUER,[∥]
RICHARD E. PELTIER,[⊥,◆]
RODNEY J. WEBER,[⊥]
SHANE M. MURPHY,[#]
JOHN H. SEINFELD,[#]
BRETT D. GROVER,[∇,¶]
DELBERT J. EATOUGH,[∇] AND
JOSE L. JIMENEZ[*,†,‡]

Cooperative Institute for Research in Environmental Sciences and Department of Chemistry and Biochemistry, Department of Atmospheric and Oceanic Sciences, University of Colorado, Boulder, Colorado, Environmental Chemistry and Technology Program, University of Wisconsin, Madison, Wisconsin, School of Earth and Atmospheric Sciences, Georgia Institute of Technology, Atlanta, Georgia, Division of Chemistry and Chemical Engineering, California Institute of Technology, Pasadena, California, and Department of Chemistry and Biochemistry, Brigham Young University, Provo, Utah

Received March 21, 2008. Revised manuscript received July 30, 2008. Accepted July 31, 2008.

Ambient sampling was conducted in Riverside, California during the 2005 Study of Organic Aerosols in Riverside to characterize the composition and sources of organic aerosol using a variety of state-of-the-art instrumentation and source apportionment techniques. The secondary organic aerosol (SOA) mass is estimated by elemental carbon and carbon monoxide tracer methods, water soluble organic carbon content, chemical mass balance of organic molecular markers, and positive matrix factorization of high-resolution aerosol mass spectrometer data. Estimates obtained from each of these methods indicate that the organic fraction in ambient aerosol is overwhelmingly secondary in nature during a period of several weeks with moderate ozone concentrations and that SOA is the single largest component of PM_1 aerosol in Riverside. Average SOA/OA contributions of 70–90% were observed during midday periods, whereas minimum SOA contributions of ~45% were observed during peak morning traffic periods. These results are contrary to previous estimates of SOA throughout the Los Angeles Basin which reported that, other than during severe photochemical smog episodes, SOA was lower than primary OA. Possible reasons for these differences are discussed.

Introduction

Aerosols are of interest due to their roles in several atmospheric processes including radiative forcing, heterogeneous reactions, and regional visibility degradation, as well as their negative impact on human health. The impact of particles on these and other atmospheric processes are dependent on particle size, the majority being strongly correlated with fine particles ($PM_{2.5}$ or PM_1), and many also depend on chemical composition. In particular, the organic fraction ("organic aerosols", OA), which typically constitutes a significant fraction of fine particle mass (*1*), is a poorly characterized aggregate of thousands of individual compounds either emitted directly in the particle-phase ("primary" OA, POA) or formed in the atmosphere from gas-to-particle conversion ("secondary" OA, SOA). Most of these compounds are not amenable to detection by currently available speciation techniques, which can identify only a small fraction of aerosol organics at the molecular level (*2*). The lack of molecular characterization of a large fraction of the mass is particularly important for SOA.

During the Study of Organic Aerosols in Riverside (SOAR-1), a variety of state-of-the-art instrumentation was assembled at the Air Pollution Research Center on the campus of the University of California-Riverside from July 18 through August 14, 2005 to investigate the chemical composition of ambient OA, representing, to our knowledge, the most complete set of OA field instruments at one location to date. Riverside is located ~80 km inland of the urban center of Los Angeles (LA). Due to its proximity to LA and the meteorology, topography, and intense emissions characteristic of the LA basin, Riverside and the surrounding areas are characterized by poor air quality, consistently rating as the worst in the United States for 24 h average fine particle concentrations both on short-term and annual bases (*3*).

Here, we estimate the fraction of SOA in fine particles using five methods including the elemental carbon (EC) and carbon monoxide (CO) tracer methods, water soluble organic carbon (WSOC) content, chemical mass balance (CMB) source apportionment of organic molecular markers (MMs), and positive matrix factorization (PMF) of high-resolution time-of-flight aerosol mass spectrometer (HR-ToF-AMS) organic mass spectra. Results obtained from each of these methods indicate that SOA contributes the majority of organic mass during a period that cannot be described as a "photochemical episode". Estimates obtained from each of these methods are higher than previous SOA estimates in locations throughout the LA Basin including Riverside and surrounding areas.

Experimental Section

General. All measurements were conducted in Riverside, California at the Air Pollution Research Center on the campus of the University of California-Riverside (33°58′18.40″N, 117°19′21.41″W). During SOAR-1 (July 18 through August 14, 2005), the Riverside area was characterized by moderate

---

[*] Corresponding author e-mail: jose.jimenez@colorado.edu.
[†] Cooperative Institute for Research in Environmental Sciences.
[‡] Department of Chemistry and Biochemistry, University of Colorado.
[§] Department of Atmospheric and Oceanic Sciences, University of Colorado.
[∥] University of Wisconsin.
[⊥] Georgia Institute of Technology.
[#] California Institute of Technology.
[∇] Brigham Young University.
[○] Currently at Paul Scherrer Institut, Switzerland.
[◆] Currently at NYU School of Medicine, Department of Environmental Medicine, Tuxedo, New York.
[¶] Currently at United States Environmental Protection Agency, National Exposure and Research Laboratory, Durham, North Carolina.

10.1021/es8008166 CCC: $40.75

ozone concentrations (average peak daily ozone concentration in Riverside = 86 ppb; range 48−141 ppb). All times refer to Pacific Standard Time.

Sunset Semicontinuous EC/OC Measurements. $PM_{2.5}$ organic carbon (OC) and elemental carbon (EC) concentrations were measured hourly using both standard (*4*) and dual-oven (*5*) Sunset semicontinuous carbon monitors (Sunset Laboratories, Tigard, OR).

Filter-Based Measurements. Filter samples were collected for source apportionment by CMB of solvent-extractable organic MMs (*2*). Details regarding particle collection, filter extraction, chemical analysis, and CMB procedures are similar to those presented in Stone et al. (*6*) with a few exceptions noted below.

Filter samples for CMB were collected daily according to the following schedule: 0400−0900; 0900−1400; 1400−1900; 1900−0400. Weekday samples collected on 7/26−7/28 and 8/2−8/4 and weekend samples collected on 7/30 and 8/6−8/7 were composited based on this schedule. For this analysis, weekday and weekend CMB source apportionment results were further composited to yield results irrespective of day of week. These samplers were not denuded. As a result, filter OC concentrations are likely inflated through adsorption of semivolatile gas-phase species. To obtain a conservative estimate of "other" OC, the results of CMB source apportionment were used in conjunction with coinciding standard Sunset OC concentrations (i.e., "other" $OC = OC_{Sunset} - $ primary OC (POC)). If we were to instead use the CMB filter OC concentrations for this estimate, other OC increases by ~7% likely as a result of these adsorption artifacts.

Particle-Into-Liquid-Sampler (PILS) Organic Measurements. Water soluble OC (WSOC) and total OC were measured by a PILS-WSOC and PILS-OC, respectively (*7*). WSOC was measured continuously every 6 minutes from 7/18−7/27 and 7/30−8/15. The PILS-OC measured total OC continuously from 7/27−7/30 at the same rate. Further details are provided elsewhere (*7*).

HR-ToF-AMS Measurements. Nonrefractory PM_1 aerosols were measured by an Aerodyne HR-ToF-AMS from 7/14−8/10. Details regarding the HR-ToF-AMS are provided elsewhere (*8*).

Data Analysis. Conversion of carbon mass concentrations. Measured concentrations of OC, WSOC, and water insoluble organic carbon (WIOC) were converted to organic mass (OM) concentrations prior to calculating SOA fractions. POC and WIOC were converted using a factor of 1.2 μgOM/μgOC, whereas secondary OC (SOC) and WSOC were converted to secondary organic mass (SOM) using a factor of 1.8 μgOM/μgOC (*9*). In Supporting Information (SI) Table S-2, we explore the sensitivity of calculated SOA/OA ratios to the applied SOM/SOC conversion factor using additional conversion factors of 1.6 and 2.0 μgOM/μgOC. As this table shows, SOA/OA ratios vary only a few percent when these alternate conversion factors are used.

HR-ToF-AMS. Unit-resolution (UMR) ToF-AMS data were analyzed using established procedures for analysis of AMS data via customized data analysis software (Squirrel) (*10*). An AMS collection efficiency (CE) of 0.5 was used for all species, typical of aerosols measured in urban locations with similar composition (*11, 12*) and verified with intercomparisons with other collocated instruments. The AMS response may be slightly biased toward POA (*13, 14*), and these SOA/OA estimates should be considered lower limits. High-resolution (HR) ToF-AMS data were analyzed using a custom data analysis module (Pika) developed in our group (*8*) in Igor (Wavemetrics, Lake Oswego, OR).

PMF Analysis. AMS organic mass spectra were analyzed by PMF to identify the major components of PM_1 OA. PMF is a variant of factor analysis with nonnegative constraints on factor elements and has been described in detail elsewhere (*15*). Its application to AMS spectra has been investigated in detail recently (*16, 17*). HR ($m/z \leq 100$ and UMR ($m/z > 100$) organic mass spectra were combined for PMF analysis. PMF2 (v4.2) was run in robust mode via a custom panel in Igor (*16*).

Lack of Important Biomass Burning (BB) Impact. Although the LA area is at times impacted by smoke from large wildfires that can increase PM_{10} levels in the basin by 300−400% (*18*), fires throughout Southern California during SOAR-1 were small in size, short in duration, and not in the vicinity of the sampling location, according to the MODIS Active Fire Detections database (http://maps.geog.umd.edu/firms/maps.asp). This is supported by measurements by a collocated aerosol time-of-flight mass spectrometer that did not observe significant PM contributions from biomass burning/biofuel combustion sources (*19*). Moreover, m/z 60 (a BB tracer) in the AMS during the study (see SI Figure S1) as well as measured concentrations of the MM levoglucosan were low during SOAR-1 (see below).

Results and Discussion

EC-Tracer Method. This method assumes that EC results predominantly from combustion processes and can be used as a tracer for primary aerosol (*20*). POC is estimated by its proportionality with EC as

$$POC = [(OC/EC)_p \times EC] + NCPOC, \qquad (1)$$

where NCPOC is noncombustion POC, and SOC is determined by difference:

$$SOC = OC - POC. \qquad (2)$$

The simple appearance of this method is belied by significant complexities associated with determining the coefficients $(OC/EC)_p$ and NCPOC in eq 1, which are traditionally obtained by linear regression analysis of EC and OC data during periods that are deemed "not impacted by SOC." NCPOC contributions (that are not correlated with EC due to similar source locations and/or activity patterns) are small relative to errors associated with the EC-tracer method (*21*). Therefore, they are lumped with SOC in the following EC-tracer calculations.

For ambient sampling, the correct $(OC/EC)_p$ should be $\Sigma(OC)/\Sigma(EC)$ for all primary sources. Therefore, OC and EC data used in the regression analysis must be carefully selected to limit contributions from SOC, which would incorrectly inflate both $(OC/EC)_p$ and POC. For areas like the LA Basin this is not trivial. Strader et al. (*22*) estimated $(OC/EC)_p$ using regression analysis of data collected in California's San Joaquin Valley and found that isolating a single period that was not impacted by photochemistry was "a dangerous proposition" due the long residence times of $PM_{2.5}$. Zhang et al. (*23*) showed that in Pittsburgh this method of estimating $(OC/EC)_p$ led to a large overestimation of POA since SOA was always a significant fraction of the OA. This technique typically neglects variations in $(OC/EC)_p$ throughout the day that can appear due to, e.g., variations in diesel and gasoline vehicle fractions, which may lead to some errors in the estimated diurnal profiles (*24*), as discussed below.

To explore the range of SOA contributions during SOAR-1, EC-tracer calculations were conducted using a range of $(OC/EC)_p$ values estimated both using available emissions inventory data and from the literature. $(OC/EC)_p$ ratios used to obtain SOA/OA estimates by the EC-tracer method, in addition to details regarding their determination, are presented in SI Table S1. $(OC/EC)_p$ estimates were calculated using available vehicle emissions inventories for the South Coast Air Basin and emission factors determined in several recent tunnel studies in California. Due to the high concentration of primary emissions observed in tunnel studies which favor partitioning of semivolatile OC to the particle

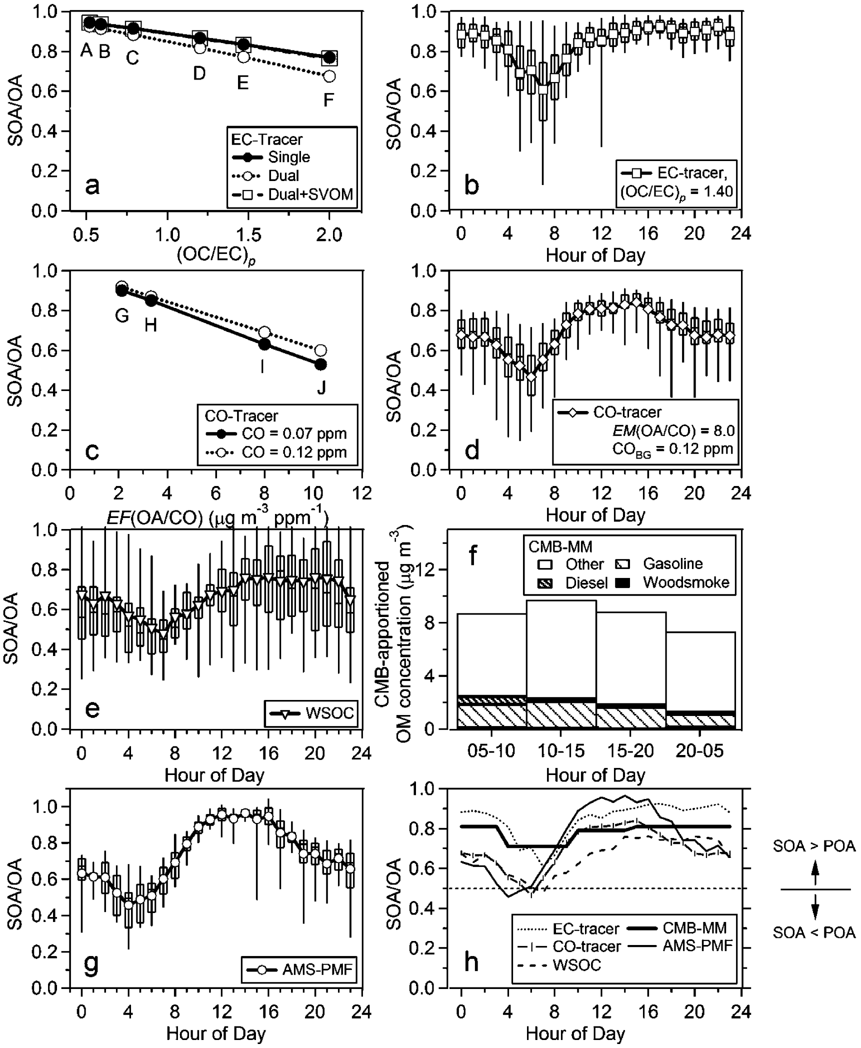

FIGURE 1. Estimated SOA/OA ratios and results of CMB OA apportionment during SOAR-1. Figure 1a shows campaign-average SOA fractions from the EC-tracer method as a function of (OC/EC)$_p$. Applied (OC/EC)$_p$ values for (A−C) were calculated using emissions ratios measured in several Caldecott Tunnel studies (*26*−*28*). Literature values for (OC/EC)$_p$ were obtained from (D) AMS spectral deconvolution (*23*), (E) radiocarbon determinations (*30*), and (F) traditional regression analysis of semicontinuous OC and EC data (*29*). Figure 1b shows the diurnal profile of SOA/OA ratios obtained from the EC-tracer method. Figures 1c and 1d show average SOA/OA ratios obtained from the CO-tracer method as a function of EF(OA/CO) and the diurnal profile of SOA/OA ratios calculated using our central estimate (EF(OA/CO)=8.0 and CO$_{BG}$ = 0.12 ppm), respectively. Figure 1e shows the diurnal profile of SOA/OA ratios obtained from the WSOC method. Figure 1f presents results of CMB OA apportionment while Figure 1g shows the diurnal profile of SOA/OA ratios obtained from PMF. Finally, Figure 1h compares SOA/OA estimates from all methods in the same plot to facilitate comparison.

phase, resulting emission factors should be considered as an upper bound to OC/EC for tunnel studies. (OC/EC)$_p$ was calculated from emissions data as follows:

$$(OC/EC)_p = [(OC_{diesel}+OC_{gasoline})/(EC_{diesel}+EC_{gasoline})] = [(EF_{OC,diesel}{}^{*}\ DFU_{diesel}) + (EF_{OC,gas}{}^{*}\ DFU_{gas})]/[(EF_{EC,diesel}{}^{*}\ DFU_{diesel}) + (EF_{EC,gas}{}^{*}\ DFU_{gas})] \quad (3)$$

where DFU$_{diesel}$ and DFU$_{gas}$ are average daily fuel use (kg day^{-1}) for diesel and gasoline, respectively, within the South Coast Air Basin for 2005 (*25*) and EF$_x$ (g OC kg^{-1} fuel) are emission factors calculated from recent tunnel studies in California (*26*−*28*).

Estimates from the ambient linear regression method are likely to constitute an upper bound for (OC/EC)$_p$ due to the difficulty involved with eliminating SOC contributions (*22*). Recent studies in both Pittsburgh (*29*) and the Los Angeles basin (*21*) report (OC/EC)$_p$ ~2. Somewhat lower (OC/EC)$_p$ estimates have been obtained by other methods including ^{14}C/^{12}C analysis of EC and OC samples (*30*) and by comparing the fraction of oxygenated OA resulting from AMS mass spectral deconvolution with average SOA fractions calculated by the EC-tracer method (*23*). Due to the use of ^{14}C/^{12}C ratios in Szidat et al. (*30*), this estimate should have lower potential inflationary errors of incorporating SOC, although it applies to a European vehicle fleet which has some differences with that of California. In Zhang et al. (*23*), equivalent SOA fractions were obtained from both methods using an (OC/EC)$_p$ = 1.20, which is equivalent to applying the regression method after subtracting the AMS-estimated SOA from the ambient OA during high POA periods. These latter literature estimates may be still higher than the tunnel studies due to the incorporation of POA from sources other than vehicle emissions, or some fast SOA formation from anthropogenic precursors (*31*).

Using each literature and emissions-based (OC/EC)$_p$ estimate, average POC and SOC concentrations were calculated using campaign-long average OC and EC concentrations measured by both Sunset instruments. Corresponding SOA estimates are shown in Figure 1a as a function of (OC/EC)$_p$. Two sets of results are shown for the dual-oven Sunset instrument showing the impact of measured semivolatile organic mass (SVOM) concentrations (*5*). As Figure 1a shows, SOA contributes a majority of $PM_{2.5}$ organic mass when averaged over the entire length of the sampling period. Conservative estimates of SOA fraction using $(OC/EC)_p = 2.0$ result in a SOA/POA ratio of ≥2:1, whereas use of a more reasonable $(OC/EC)_p \sim 1.4$ gives corresponding ratios of ≥4:1. Using $(OC/EC)_p$ ratios from tunnel studies results in a SOA/POA ratio ≥4.5:1. The diurnal plot of SOA/OA ratios calculated from the EC-tracer method using EC/OC data from the standard Sunset instrument and an $(OC/EC)_p = 1.4$ is shown in Figure 1b. This calculation provides an overall average SOA/OA ratio 84 ± 18%, with a minimum during the morning rush hour as expected.

CO-Tracer Method. The CO-tracer method is analogous to the EC-tracer method and has been used recently to estimate the fraction of SOA in PM_1 using collocated measurements of AMS organics and CO (*32*). Similar to the EC-tracer method, the CO-tracer method apportions POA mass using a tracer of primary emissions along with an estimated emissions ratio. However, due to different OA/CO and OA/EC emission ratios of different sources such as diesel and gasoline vehicles (*24*), the results of the CO-tracer method have some differences with those from the EC-tracer method. These differences are an indication of the uncertainty in the estimates for this type of simplified method. POA concentrations are calculated using

$$POA = (OA/CO)_p \times \Delta CO + NCPOC \qquad (4)$$

where ΔCO is the CO enhancement above background (i.e., $CO_i - CO_{BG}$) and $(OA/CO)_p$ is the POA to CO emissions ratio. SOA concentrations are estimated as the difference between the measured OA and the summed POA similar to eq 2 above.

$(OA/CO)_p$, like $(OC/EC)_p$, needs to be estimated with similar methods, e.g., from regression analysis of "less processed" air (i.e., air masses where OA concentrations are thought to be dominated by primary combustion sources). This ratio has previously been estimated in a variety of locations including Pittsburgh (*23*), New England (*33*), and Tokyo (*32*) with values ranging from 4.3−14.4 $\mu g\ m^{-3}$ OA ppm^{-1} CO. The minimum within this range was determined by Zhang et al. (*23*) based on regression of ambient CO and hydrocarbon-like aerosol obtained from deconvolution of AMS mass spectra and is higher than OA/CO emission ratios of 2.13 (*26*) and 3.33 $\mu g\ m^{-3}\ ppm^{-1}$ (*28*) obtained from California tunnel studies. The regression of total OA during high POA periods yields an $(OA/CO)_p = 10.3\ \mu g\ m^{-3}\ ppm^{-1}$ during SOAR-1. As with the EC-tracer method, estimates based on total ambient OA are very likely biased high due to the presence of some SOA that also shows strong correlation with anthropogenic tracers (*33*) and should be considered upper limits. We use a ratio of 8.0 $\mu g\ m^{-3}\ ppm^{-1}$ and $CO_{BG} = 0.12$ ppm (*34*) for our central estimate, and explore the sensitivity to the more conservative estimate obtained using a ratio of 10.3 and $CO_{BG} = 0.07$ ppm. We neglect changes in $(OA/CO)_p$ with time-of-day that can introduce some error in the diurnal profiles (*24*). CO produced through oxidation of volatile organic compounds is estimated to make a minimal contribution (~1%) to excess CO in the South Coast Air Basin (*35*).

Figure 1c shows SOA/OA ratios resulting from the CO-tracer method as a function of $(OA/CO)_p$ at background CO concentrations of 0.07 and 0.12 ppm. As this plots shows, the CO-tracer method again indicates that OA measured during SOAR-1 is dominated by SOA. The average SOA/OA ratio obtained from the central estimate is 69% ± 24%. This estimate decreases by ~16% when CO-tracer method calculations were repeated using the more conservative assumptions. Similarly, using the average ratio from tunnel studies and $CO_{BG} = 0.12$ increases the SOA/OA ~20% compared to the central estimate. The diurnal profile of SOA/OA ratios calculated using our central estimate of the CO-tracer method is presented in Figure 1d. Maximum SOA/OA ratios >80% are observed during mid-day hours (1100−1600) and later steadily decline to a midnight value of ~67%. As expected, minimum contributions from SOA were observed during the morning rush hour with an absolute minimum of ~47% at 0600.

SOA Estimate from WSOC Content. In polluted regions, compounds comprising WSOC are either mainly emitted from BB sources or formed via secondary atmospheric processes (*36*). SOA species are polar and typically highly oxygenated, leading to much higher water solubility than for reduced anthropogenic POA species. Due to the small fraction of BB OA during SOAR-1, most of the WSOC should be due to SOA species. In order to accurately use WSOC as a surrogate for SOC, measured WSOC concentrations must be adjusted to account for the water-insoluble fraction of oxygenated organic carbon (OOC). A conservative estimate of this fraction is obtained here from Kondo et al. (*37*) where it was estimated that 6−26% of summer OOC in Tokyo was water-insoluble based on direct comparisons between PILS-WSOC and Quadrupole AMS measurements. However, water- insoluble SOA fractions as large as 60% have recently been reported (*38*) which if applicable in CA would result in a low bias in our SOA estimates by this technique.

A WSOC/OC ratio of 0.56 ± 0.05 was obtained from PILS-WSOC and PILS-OC measurements during SOAR-1 (*7*). We estimate the SOA fraction using this ratio corrected for water-insoluble OOA content and converted to OM using factors discussed above. A conservative 24 h average SOA/OA estimate of 66 ± 8% is obtained using the 6% water-insoluble OOC correction, which increases by ~9% when the 26% water-insoluble OOC correction is instead applied. The diurnal profile of SOA/OA estimates from the WSOC method using the 6% water-insoluble OOC correction is shown in Figure 1e. A global minimum of 48% is obtained at 0700 with maximum values of ~75% occurring at mid-day. A final concern is the potential contribution of highly water soluble organics from BB to WSOC concentrations, which would artificially increase this SOA estimate. As discussed previously, the impact of BB throughout the LA basin during SOAR-1 was small. Using the results of CMB analysis (below) we estimate that the contribution of BB to WSOC and total OA is ≤1% using a WSOC/OC emissions ratio of 0.71 (*39*). As a result, the estimate for SOA fraction obtained from this method would change little if the BB contribution were to be subtracted.

CMB of Organic Molecular Markers. CMB models are based on the mass conservation of individual organic species. The mass conservation equations are written as the matrix product of unknown time series of source contributions and known source profiles equaling the time series of known concentrations of a set of molecular marker species observed in ambient aerosol and are solved with the effective variance least-squares method. CMB models have been used to apportion source contributions to ambient $PM_{2.5}$ in numerous locations including the LA Basin (e.g., refs *2, 6*).

Here CMB is applied to selected OA tracer species that are solvent extractable and elutable from a gas chromatography (GC) column, which applies to only a limited amount of particle-associated organic compounds (*2*). However, this small subset is sufficient to act as tracers of major primary sources (*2*), including fossil fuel, coal, natural gas, and biomass combustion, vegetative detritus, and meat smoke. Hopanes and *n*-alkanes were included in the CMB model as markers for fossil fuel combustion (*40*). Markers for woodsmoke including levoglucosan (*41*) were also measured and included in the CMB model. Markers for coal, natural gas combustion, meat smoke, and vegetative detritus were either not observed or negligible and were not included. The measured concentrations of selected $PM_{2.5}$ organic marker species included in the CMB model are shown in SI Figure S2 by filter composite period. On average, the concentrations of all quantified organic species and CMB tracer species compose <5 and <0.5% of total OA, respectively.

Molecular markers for SOA, comprised of organic compounds formed in the atmosphere through condensation or gas-to-particle conversion, are difficult to quantify with GC analysis and are not typically apportioned by CMB models. An upper bound estimate of SOA, however, can be obtained by difference:

$$SOA_{CMB} = OA - \sum (POA_i) \tag{5}$$

where $\Sigma(POA_i)$ is the sum of the POA apportioned to all sources (*2*).

Results of CMB OA apportionment are shown in Figure 1f. For each composite period, CMB apportioned >95% of POC to fossil fuel emissions, with the majority (~64%) being attributed to emissions from gasoline vehicles. The small remainder (<5%) of the POC in each composite period was apportioned to BB (~0.1 $\mu g\,m^{-3}$ daily average). In each period, the total CMB-apportioned POA makes up a relatively small fraction of measured $PM_{2.5}$ OA. In contrast, the "other" organics consistently contributes the largest amount of mass (77%; range 72−83%). Recent studies have indicated that the bulk of this fraction is SOA, which is also consistent with the estimates of the four other methods presented here. For example, CMB source apportionment of $PM_{2.5}$ OA in six southeastern United States locations observed highest contributions of "other" organic in all locations during July, coinciding with peak photochemical activity (*42*). Additionally, strong correlations have been observed between this fraction and the sum of secondary inorganics (*42*) and ambient WSOC concentrations (*6*).

PMF Analysis of HR-ToF-AMS Data. In contrast to most of the methods discussed above that apportion SOA as the difference between measured OA and apportioned POA, PMF explicitly identifies individual OA components. PMF and similar advanced factor analysis models have previously used Quadrupole AMS data to determine OA sources in urban regions of Pittsburgh and Zurich, Switzerland (*16, 17*). The use of HR data results in greater differentiation between the spectra of the OA components, which has been shown to enhance AMS OA component separation using PMF (*16*).

The number of factors identified in the PMF solution was selected by examining both mathematical PMF diagnostics and interpretability of the identified factors based on similarity with AMS source spectra and time series of independent tracers (*16, 17, 43*). Reduced (hydrocarbon-like, HOA) components were classified as primary, OOA components were classified as secondary, and one small (~5% contribution to PM_1 OA mass) component was classified as "other" based on these comparisons (*16, 17, 23, 44*). Finally, the mass concentration of SOA was calculated as the sum of individual secondary factor mass concentrations. Some fresh SOA can have a reduced spectrum and may be incorrectly classified as POA by this method (*45*).

Over the entire sample period, the average SOA/OA ratio obtained from PMF analysis is 74 ± 19%. The diurnal profile of SOA/OA ratios from PMF-AMS analysis is shown in Figure 1g. Minimum SOA/OA ratios ~45% are again observed during the morning rush hour period. Overall, this profile is very similar to that obtained with the CO-tracer method. However the EC-tracer method apportions SOA slightly differently throughout the evening/night, with higher SOA/OA ratios during those periods. This may result from higher $(OC/EC)_p$ during the night due to reduced diesel traffic at that time (*24*).

In order to facilitate comparison, Figure 1h shows the diurnal profiles of SOA/OA estimated by all methods. Diurnal cycles of these ratios are similar with maximum SOA/OA ratios of 70−90% estimated by each method during the early afternoon. Minimum SOA/OA ratios obtained from each method do not fall below 45% during any 1 h period. The differences in the diurnal profiles are indicative of current uncertainties in the estimation of SOA from field measurements.

Dominant contributions of SOA to OA also do not appear to be limited to distant locations at the eastern part of the LA basin. AMS mass spectra from Riverside and Pasadena (14 km NNE of downtown LA) exhibit a high degree of similarity and suggest that Pasadena OA is also characterized by high SOA/OA ratios. SI Figure S3 compares Riverside UMR OA mass spectra averaged from 7/28 to 8/3 with that measured by a C-ToF-AMS at the California Institute of Technology (Caltech) in Pasadena over the same time period. The degree of OA oxidation, estimated using the ratio of m/z 44 (oxidized OA marker fragment) to total organics (*46*) is similar (even slightly higher in Pasadena), indicating a high degree of oxidation in OA observed in both locations, likely explained by rapid SOA formation (*31*). In support of this observation, we note that although estimates by Pandis et al. (*47*) are significantly lower than those obtained during SOAR-1, similar SOA contributions to total organics were calculated for Rubidoux and Burbank, which are located near Riverside and Pasadena, respectively. Back-trajectories shown in SI Figure S4 indicate that air masses arriving at each location at 1:00 p.m. were transported from the west through the Los Angeles urban area and spent several hours to a day over the urban area before their arrival at either measurement site.

Comparison with Previous Estimates of SOA in this Area. Numerous studies have previously estimated the SOA in the LA Basin using a variety of methods including modeling (*47−51*), CMB-MM (*2, 52*), and the EC-tracer method (*20, 21, 53*). Figure 2 presents several previous estimates of SOA/OA in this region along with the five estimates from this study.

There is considerable variation in SOA estimates reported by previous studies much of which is likely due to differences in sampling season, location, and duration. Common to all these previous studies, however, is that POA contributes the majority of OA over extended periods. Unlike the current study, SOA/OA ratios >50% have previously been reported to occur only during severe photochemical smog events (SPSE), characterized by ozone concentrations in excess of ≥200 ppb. Schauer et al. (*52*) reported results of CMB source apportionment on filter samples collected throughout the LA basin during a two-day photochemical smog event in 1993. The eastern-most sampling location was Claremont, California, ~50 km inland of LA where CMB apportioned ~75% of measured OA as SOA. Similarly, Turpin et al. (*20*) observed several photochemical smog events in Claremont. During the events observed by Turpin et al., SOA/OA ratios were estimated to be greater than 50% for a few hours following the daily maximum ozone concentration. Both of these studies reported the predominance of SOA over short time periods with high photochemistry, which span between a few hours and two days. If we exclude these limited photochemical events, however, previous summer studies taken together indicate an average SOA fraction below 50% (*20, 21, 47, 53*). However, SOA fractions estimated during the multiweek SOAR-1 study are substantially higher (74% based on the average of the five methods) than estimated by these previous studies despite the fact that ozone concentrations in this part of the basin were not significantly elevated during SOAR-1.

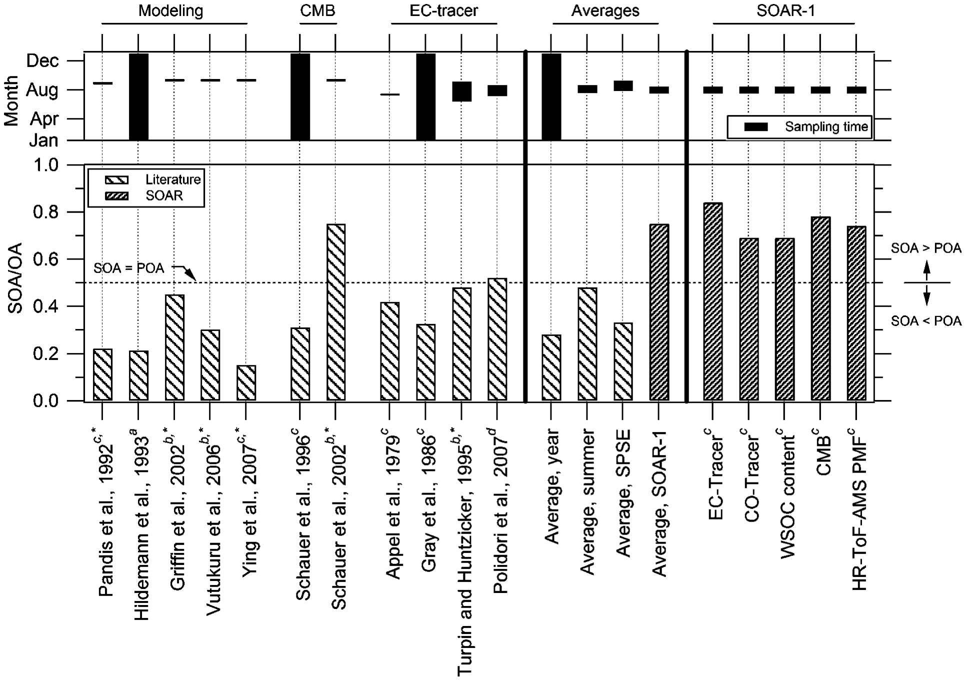

FIGURE 2. Comparison of SOA/OA ratios determined during SOAR-1 with previous measurements throughout the Eastern LA Basin using a range of analytical methods. The bottom shows the reported SOA fraction, whereas the top shows the time and duration of sampling corresponding to each estimate. Subscript letters indicate sampling location *a*) multiple locations; *b*) Claremont/Azusa; *c*) Riverside/Rubidoux; and *d*) undisclosed location (due to confidentiality) ~50 km east of LA, and * indicates an estimate obtained during a photochemical smog event.

Different SOA estimates between SOAR-1 and previous studies may have a number of underlying explanations including (1) atypical atmospheric conditions during the SOAR-1 campaign; (2) problems in methods used to obtain previous SOA estimates; and (3) genuine changes in organic aerosol sources. Differences are not likely due to anomalous conditions during SOAR-1. SI Figure S5 presents daily average $PM_{2.5}$, ozone, CO, and NO_x concentrations measured in Rubidoux (~10 km west of Riverside) along with total acres burned in fire events in Riverside and San Bernardino Counties for the period 7/15 to 8/15/2000−2006, whereas Figures S6 and S7 in the SI compare the meteorological conditions for these same periods. For 2005, ozone is very similar to previous years suggesting a likely similar contribution of SOA (*54*). While CO is lower, NO_x is very similar to previous years, indicating that the POA contribution was not drastically smaller than in 2000−2004. Since the main source of CO is gasoline vehicles, if we increase their CMB-estimated POA contribution proportional to the difference in CO, we would obtain a CO-corrected SOA estimate of 68% according to CMB, which should be treated as a lower limit since gasoline vehicles are also an important source of NO_x, and since the additional gasoline emissions would also increase SOA.

Some of this difference however can be explained by problems in the methods applied to obtain the previous estimates. For instance, large uncertainties in the Pandis et al. (*47*) SOA estimates were attributed to understated basin-wide emissions of gas-phase organics and discrepancies in experimentally determined SOA yields. Doubling the VOC emissions increased SOA fractions in Claremont by a factor of 2.3 and improved the correlation between projected and measured ozone concentrations. With regard to SOA yields, it has been shown that model predictions based on simulation chamber yields dramatically underestimate SOA formation in the polluted atmosphere (*31*). Recently determined SOA yields (e.g., ref *55*) close the gap somewhat, but a significant discrepancy still remains. Scaling up the modeling SOA estimates (*47*−*51*) by the measurement/model discrepancies summarized in ref *31* would produce SOA fractions of the order of those in this study. Additionally, estimates based on EC-tracer method calculations could be biased low due to difficulties estimating $(OC/EC)_p$ with the ambient regression method. Previous studies using the EC-tracer method in the LA basin have obtained SOA/OA ≤ 50% using $(OC/EC)_p \geq 2$. As discussed earlier, this is likely an overestimate with more realistic values being ~1.4 or lower. Recalculating the results of Polidori et al. (*21*) using an $(OC/EC)_p = 1.4$ increases the SOA/OA to ~65%. Recalculating results from other studies which applied the EC-tracer method is not possible due to a lack of reported data.

Another possible reason for the observed differences is that the fraction of SOA in the LA basin may have increased with time via, e.g., more efficient POA emissions reduction (due to targeted policies such as vehicle emission controls), than reduction of SOA precursors (*28*). Although VOCs generally have been targeted by emission control policies with the main goal of reducing O_3 formation, the dominant precursors and pathways of SOA formation in urban areas are very unclear at present (*31*), so it is difficult to evaluate the impact of previous air quality improvement policies in SOA relative to POA.

Our estimates from SOAR-1 indicate that the composition of OA at the eastern part of the LA Basin is dominated by SOA by a wide margin, and that these results likely extend to the western part of the basin as well. Contributions from POA are significantly smaller and are similar to SOA only during the morning rush hour. These high contributions from SOA also occurred absent severe photochemical smog events. Source apportionment of OA is important to regulatory strategies involved with protecting air quality and human health. These efforts have put more emphasis on controlling direct POA emissions than emissions of SOA precursor gases. Our results strongly suggest that this strategy should be reconsidered due to the overwhelming contribution of SOA to OA during the summer in the LA basin.

Acknowledgments

We acknowledge funding provided by U.S. Environmental Protection Agency (EPA) STAR grants RD832161010 and R831080, National Science Foundation (NSF) grant ATM-0449815, and NSF/UCAR grant S05-39607. P.F.D. and I.M.U. were supported by EPA Fellowship FP-9165081 and NASA Fellowship NNG05GQ50H, respectively. We also thank Megan McKay and Allen Goldstein for the use of their CO measurements in the CO-tracer calculations, and the rest of the Jimenez group and Aerodyne Research for support in the field and helpful discussions. We would also like to thank Paul Ziemann and the Air Pollution Research Center for hosting the SOAR-1 study. The United States Environmental Protection Agency through its Office of Research and development collaborated in the research described here. It has been subjected to Agency review and approved for publication. Mention of trade names or commercial products does not constitute endorsement or recommendation for use.

Supporting Information Available

Figures S1–S7 and Tables S1 and S2. This material is available free of charge via the Internet at http://pubs.acs.org.

Literature Cited

(1) Zhang, Q.; et al. Ubiquity and dominance of oxygenated species in organic aerosols in anthropogenically-influenced Northern Hemisphere midlatitudes *Geophys. Res. Lett.* **2007**, *34*, L13801, doi: 10.1029/2007GL029979.

(2) Schauer, J. J.; et al. Source apportionment of airborne particulate matter using organic compounds as tracers. *Atmos. Environ.* **1996**, *30*, 3837–3855.

(3) American Lung Association's State of the Air, 2007, http://lungaction.org/reports/sota07_cities.html.

(4) Synder, D. C.; Schauer, J. J. An inter-comparison of two black carbon aerosol instruments and a semi-continious elemental carbon instrument in the urban environment. *Aerosol Sci. Technol.* **2007**, *41*, 463–474.

(5) Grover, B. D.; et al. Semi-continuous mass closure of the major components of fine particulate matter in Riverside, CA. *Atmos. Environ.* **2008**, *42*, 250–260.

(6) Stone, E. A.; et al. Source apportionment of fine organic aerosol in Mexico City during the MILAGRO Experiment 2006. *Atmos. Chem. Phys.* **2008**, *8*, 1249–1259.

(7) Peltier, R. E.; et al. Investigating a liquid-based method for online organic carbon detection in atmospheric particles. *Aerosol Sci. Technol.* **2007**, *41*, 1117–1127.

(8) DeCarlo, P. F.; et al. Field-deployable, high-resolution, time-of-flight aerosol mass spectrometer. *Anal. Chem.* **2006**, *78*, 8281–8289.

(9) Turpin, B. J.; Lim, H. J. Species contributions to PM2.5 mass concentrations: Revisiting common assumptions for estimating organic mass. *Aerosol Sci. Technol.* **2001**, *35*, 602–610.

(10) Sueper, D., ToF-AMS High Resolution Analysis Software—Squirrel, http://cires.colorado.edu/jimenez-group/ToFAMSResources/ToFSoftware/SquirrelInfo/.

(11) Salcedo, D.; et al. Characterization of ambient aerosols in Mexico City during the MCMA-2003 campaign with Aerosol Mass Spectrometry: results from the CENICA Supersite. *Atmos. Chem. Phys.* **2006**, *6*, 925–946.

(12) Canagaratna, M.; et al. Chemical and microphysical characterization of ambient aerosols with the Aerodyne Aerosol Mass Spectrometer. *Mass Spectrom. Rev.* **2007**, *26*, 185–222.

(13) Slowik, J. G.; et al. Particle morphology and density characterization by combined mobility and aerodynamic diameter measurements. Part 2: Application to combustion-generated soot aerosols as a function of fuel equivalence ratio. *Aerosol Sci. Technol.* **2004**, *38*, 1206–1222.

(14) Jimenez, J. L.; et al. Ambient aerosol sampling using the Aerodyne Aerosol Mass Spectrometer *J. Geophys. Res.-Atmos* **2003**, *108* 8425, doi: 10.1029/2001JD001213.

(15) Paatero, P.; Tapper, U. Positive matrix factorization-A nonnegative factor model with optimal utilization of error-estimates of data values. *Environmetrics* **1994**, *5*, 111–126.

(16) Ulbrich, I.; et al. Interpretation and of organic components from Positive Matrix Factorization of Aerosol Mass Spectrometric data. *Atmos. Phys. Chem. Discussions* **2008**, *8*, 6729–6791.

(17) Lanz, V. A.; et al. Source apportionment of submicron organic aerosols at an urban site by factor analytical modelling of aerosol mass spectra. *Atmos. Chem. Phys.* **2007**, *7*, 1503–1522.

(18) Phuleria, H. C.; et al. Air quality impacts of the October 2003 Southern California wildfires *J. Geophys. Res.-Atmos.* **2005**, *110*, D07S20, doi: 10.1029/2004JD004626.

(19) Prather, K. A. personal communication. **2007**.

(20) Turpin, B. J.; Huntzicker, J. J. Identification of secondary organic aerosol episodes and quantitation of primary and secondary organic aerosol concentrations during SCAQS. *Atmos. Environ.* **1995**, *29*, 3527–3544.

(21) Polidori, A.; et al. Indoor/outdoor relationships, trends, and carbonaceous content of fine particulate matter in retirement homes of the Los Angeles basin. *J. Air Waste Manage Assoc.* **2007**, *57*, 366–379.

(22) Strader, R.; et al. Evaluation of secondary organic aerosol formation in winter. *Atmos. Environ.* **1999**, *33*, 4849–4863.

(23) Zhang, Q.; et al. Hydrocarbon-like and oxygenated organic aerosols in Pittsburgh: insights into sources and processes of organic aerosols. *Atmos. Chem. Phys.* **2005**, *5*, 3289–3311.

(24) Harley, R. A.; et al. Changes in motor vehicle emissions on diurnal to decadal time scales and effects on atmospheric composition. *Environ. Sci. Technol.* **2005**, *39*, 5356–5362.

(25) CARB Emissions data for South Coast Air Basin, 2005, http://www.arb.ca.gov/ei/emissiondata.html.

(26) Kirchstetter, T. W.; et al. On-road measurement of fine particle and nitrogen oxide emissions from light- and heavy-duty motor vehicles. *Atmos. Environ.* **1999**, *33*, 2955–2968.

(27) Allen, J. O.; et al. Emissions of size-segregated aerosols from on-road vehicles in the Caldecott Tunnel. *Environ. Sci. Technol.* **2001**, *35*, 4189–4197.

(28) Ban-Weiss, G. A.; et al. Long-term changes in emissions of nitrogen oxides and particulate matter from on-road gasoline and diesel vehicles. *Atmos. Environ.* **2008**, *42*, 220–232.

(29) Cabada, J. C.; et al. Estimating the secondary organic aerosol contribution to PM$_{2.5}$ using the EC tracer method. *Aerosol Sci. Technol.* **2004**, *38*, 140–155.

(30) Szidat, S.; et al. Contributions of fossil fuel, biomass-burning, and biogenic emissions to carbonaceous aerosols in Zurich as traced by C-14 *J. Geophys. Res., [Atmos]* **2006**, *111*, D07206, doi: 10.1029/2005JD006590.

(31) Volkamer, R.; et al. Secondary organic aerosol formation from anthropogenic air pollution: Rapid and higher than expected *Geophys. Res. Lett.* **2006**, *33*, 17, L17811, doi: 10.1029/2006GL026899.

(32) Takegawa, N.; et al. Seasonal and diurnal variations of submicron organic aerosol in Tokyo observed using the Aerodyne aerosol mass spectrometer *J. Geophys. Res., [Atmos]* **2006**, *111*, D11206, doi: 10.1029/2005JD006515.

(33) de Gouw, J. A.; et al. Budget of organic carbon in a polluted atmosphere: Results from the New England Air Quality Study in 2002 *J. Geophys. Res., [Atmos]* **2005**, *110*, D16305, doi: 10.1029/2004JD005623.

(34) Kleeman, M. J.; et al. Source contributions to the size and composition distribution of atmospheric particles: Southern California in September 1996. *Environ. Sci. Technol.* **1999**, *33*, 4331–4341.

(35) Griffin, R. J.; et al. Contribution of gas phase oxidation of volatile organic compounds to atmospheric carbon monoxide levels in two areas of the United States *J. Geophys. Res., [Atmos]* **2007**, *112*, D10S17, doi: 10.1029/2006JD007602.

(36) Weber, R. J.; et al. A study of secondary organic aerosol formation in the anthropogenic-influenced southeastern United States *J. Geophys. Res., [Atmos]* **2007**, *112*, D13302, doi: 10.1029/2007JD008408.

(37) Kondo, Y.; et al. Oxygenated and water-soluble organic aerosols in Tokyo *J. Geophys. Res., [Atmos]* **2007**, *112*, D01203, doi: 10.1029/2006JD007056.

(38) Favez,O.; et al. Significant formation of water-insoluble secondary organic aerosol in semi-arid urban environment *Geophys. Res. Lett.* **2008** *35*, L15801, doi: 10.1029/20086L034446.

(39) Sannigrahi, P.; et al. Characterization of water-soluble organic carbon in urban atmospheric aerosols using solid-state C-13 NMR spectroscopy. *Environ. Sci. Technol.* **2006**, *40*, 666–672.

(40) Rogge, W. F.; et al. Sources of fine organic aerosol 2. Noncatalyst and catalyst-equipped automobiles and heavy-duty diesel trucks. *Environ. Sci. Technol.* **1993**, *27*, 636–651.

(41) Simoneit, B. R. T.; et al. Levoglucosan, a tracer for cellulose in biomass burning and atmospheric particles. *Atmos. Environ.* **1999**, *33*, 173–182.

(42) Zheng, M.; et al. Source apportionment of PM$_{2.5}$ in the southeastern United States using solvent-extractable organic

compounds as tracers. *Environ. Sci. Technol.* **2002**, *36*, 2361–2371.

(43) Reff, A.; et al. Receptor modeling of ambient particulate matter data using positive matrix factorization: Review of existing methods. *J. Air Waste Manage Assoc.* **2007**, *57*, 146–154.

(44) Zhang, Q.; et al. Deconvolution and quantification of hydrocarbon-like and oxygenated organic aerosols based on aerosol mass spectrometry. *Environ. Sci. Technol.* **2005**, *39*, 4938–4952.

(45) Kroll, J. H. Evolution of Diesel Exhaust Aerosol in an Urban Environment, EOS Transactions AGU, Fall Meeting Supp., paper A31E-02, 2007.

(46) Aiken, A.; et al. O/C and OM/OC ratios of primary, secondary, and ambient organic aerosols with high resolution time-of-flight mass spectrometry. *Environ. Sci. Technol.* **2008**, *42*, 4478–4485.

(47) Pandis, S. N.; et al. Secondary organic aerosol formation and transport. *Atmos. Environ. A* **1992**, *26*, 2269–2282.

(48) Hildemann, L. M.; et al. Mathematical-modeling of urban organic aerosol—Properties measured by high-resolution gas-chromatography. *Environ. Sci. Technol.* **1993**, *27*, 2045–2055.

(49) Griffin, R. J.; et al. Secondary organic aerosol - 3. Urban/regional scale model of size- and composition-resolved aerosols *J. Geophys. Res., [Atmos]* **2002**, *107*, 4334, doi: 10.1029/2001JD000544.

(50) Vutukuru, S.; et al. Simulation and analysis of secondary organic aerosol dynamics in the South Coast Air Basin of California *J. Geophys. Res., [Atmos]* **2006**, *111*, 13, D10S12, doi: 10.1029/2005JD006139.

(51) Ying, Q.; et al. Verification of a source oriented externally mixed air quality model during a severe photochemical smog episode. *Atmos. Environ.* **2007**, *41*, 1521–1538.

(52) Schauer, J. J.; et al. Source reconciliation of atmospheric gas-phase and particle-phase pollutants during a severe photochemical smog episode. *Environ. Sci. Technol.* **2002**, *36*, 3806–3814.

(53) Appel, B. R.; et al. Analysis of carbonaceous material in Southern California atmospheric aerosols. 2. *Environ. Sci. Technol.* **1979**, *13*, 98–104.

(54) Herndon, S. C.; et al. The correlation of secondary organic aerosol with odd oxygen in a megacity outflow *Geophys. Res. Lett.* **2007**, *35*, L15804, doi: 10.1029/2008Gl034058.

(55) Ng, N. L.; et al. Secondary organic aerosol formation from *m*-xylene, toluene, and benzene. *Atmos. Chem. Phys.* **2007**, *7*, 3909–3922.

ES8008166

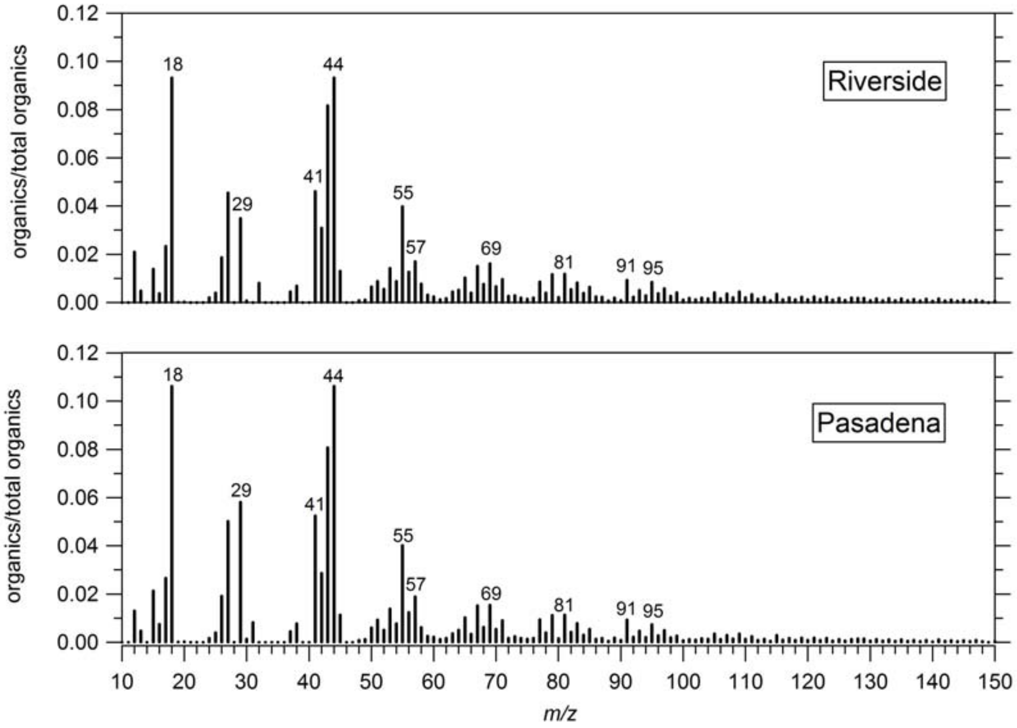

Figure S3. Comparison of Riverside and Pasadena (Caltech) AMS organic mass spectra (see text). Spectra are normalized to the total organics signal to facilitate comparison.

Appendix C

Aerosol Hygroscopicity in the Marine Atmosphere: A Closure Study Using High-Time Resolution, Multiple-RH DASH-SP and Size-Resolved C-ToF-AMS Data*

---

*This chapter is reproduced by permission from “Aerosol hygroscopicity in the marine atmosphere: A closure study using high-time-resolution, multiple-RH DASH-SP and size-resolved C-ToF-AMS data.” S. P. Hersey, A. Sorooshian, S. M. Murphy**,** R. C. Flagan, J. H. Seinfeld, *Atmospheric Chemistry and Physics,* 9 (7), 2543-2554, 2009.

Atmos. Chem. Phys., 9, 2543–2554, 2009
www.atmos-chem-phys.net/9/2543/2009/

Atmospheric Chemistry and Physics

Aerosol hygroscopicity in the marine atmosphere: a closure study using high-time-resolution, multiple-RH DASH-SP and size-resolved C-ToF-AMS data

S. P. Hersey, A. Sorooshian, S. M. Murphy, R. C. Flagan, and J. H. Seinfeld

Departments of Chemical Engineering and Environmental Science and Engineering, Caltech, Pasadena, CA 91125, USA

Received: 14 July 2008 – Published in Atmos. Chem. Phys. Discuss.: 4 September 2008
Revised: 17 November 2008 – Accepted: 24 March 2009 – Published: 7 April 2009

Abstract. We have conducted the first airborne hygroscopic growth closure study to utilize data from an Aerodyne compact Time-of-Flight Aerosol Mass Spectrometer (C-ToF-AMS) coupled with size-resolved, multiple-RH, high-time-resolution hygroscopic growth factor (GF) measurements from the differential aerosol sizing and hygroscopicity spectrometer probe (DASH-SP). These data were collected off the coast of Central California during seven of the 16 flights carried out during the MASE-II field campaign in July 2007. Two of the seven flights were conducted in airmasses characterized by continental origin. These flights exhibited elevated organic volume fractions ($VF_{organic}$=0.56±0.19, as opposed to 0.39±0.20 for all other flights), corresponding to significantly suppressed GFs at high RH (1.61±0.14 at 92% RH, as compared with 1.91±0.07 for all other flights), more moderate GF suppression at intermediate RH (1.53±0.10 at 85%, compared with 1.58±0.08 for all other flights), and no measurable GF suppression at low RH (1.31±0.06 at 74%, compared with 1.31±0.07 for all other flights). Organic loadings were slightly elevated in above-cloud aerosols, as compared with below-cloud aerosols, and corresponded to a similar trend of significantly suppressed GF at high RH, but more moderate impacts at lower values of RH. A hygroscopic closure based on a volume-weighted mixing rule provided good agreement with DASH-SP measurements (R^2=0.78). Minimization of root mean square error between observations and predictions indicated mission-averaged organic GFs of 1.22, 1.45, and 1.48 at 74, 85, and 92% RH, respectively. These values agree with previously reported values for water-soluble organics such as dicarboxylic and multifunctional acids, and correspond to a highly oxidized, presumably water-soluble, organic fraction (mission-averaged O:C=0.92±0.33). Finally, a backward stepwise linear regression revealed that, other than RH, the most important predictor for GF is $VF_{organic}$, indicating that a simple emperical model relating GF, RH, and the relative abundance of organic material can provide accurate predictions (R^2=0.77) of hygroscopic growth for the California coast.

1 Introduction

Atmospheric aerosols change size with fluctuations in relative humidity, with a magnitude dictated by chemical composition. Because this hygroscopic response determines particle size, it influences direct climate forcing attributed to aerosols. Further, subsaturated hygroscopic growth factor ($D_{p,\,\mathrm{wet}}/D_{p,\,\mathrm{dry}}$) is strongly correlated with CCN activity (Prenni et al., 2001). Given the importance of aerosol water uptake on both the direct and indirect light scattering properties of aerosols, incomplete understanding of aerosol hygroscopicity has been identified as a major limitation in estimations of climate forcing (IPCC, 2007).

With a firm foundational understanding of hygroscopic properties of inorganic aerosol constituents, there has been a significant shift in focus toward organic hygroscopicity in the last decade, as a number of theoretical (e.g., Clegg and Seinfeld, 2006; Topping et al., 2005a,b), laboratory (Peng et al., 2001; Choi and Chan, 2002a,b; Peng and Chan, 2001; Sjogren et al., 2007; Virkkula et al., 1999; Cruz and Pandis, 2000; Prenni et al., 2001, 2007, 2003; Cocker et al., 2001a,b; Hameri et al., 2002; Saathoff et al., 2003; Petters et al., 2006; Varutbangkul et al., 2006; Sjogren et al., 2007; Moore and Raymond, 2008; Rood et al., 1985; Carrico et al., 1998, 2000; Dougle et al., 1998; Magi and Hobbs, 2003; Kim et al., 2006; Kreisberg et al., 2001; Hegg et al., 2006;

Correspondence to: J. H. Seinfeld
(seinfeld@caltech.edu)

Massling et al., 2007), and chamber (e.g., Ansari and Pandis, 2000; Cocker et al., 2001a,b; Duplissy et al., 2008) studies have sought to address how the presence of organics affects the water uptake characteristics of atmospheric aerosol. Despite advances in understanding of hygroscopic characteristics of organic-containing particles, measurements of aerosol hygroscopicity in field campaigns have remained relatively sparse.

Closure studies, which attempt to reconcile simultaneously measured hygroscopic and chemical data, link laboratory studies of hygroscopicity, theoretical models for water uptake, and field measurements of aerosol-water interactions. The standard method for predicting hygroscopic growth from composition data is based on volume-weighted water uptake by the individual chemical constituents. While it is usually possible to predict water uptake for the inorganic fraction of atmospheric aerosols, the wealth of organic species in the atmosphere, combined with limited understanding of organic aerosol hygroscopicity, has led investigators to assign the water uptake of organics as the particle growth not explained by inorganic constituents (e.g., Malm et al., 2005).

An important approach in hygroscopicity closure is to combine ambient measurements of water uptake with simultaneous, detailed chemical measurements from the Aerodyne Aerosol Mass Spectrometer (AMS). One notable ground-based study in an urban atmosphere (Gysel et al., 2007) used chemical data from the AMS to make volume-weighted predictions of hygroscopic growth factor (GF), providing good agreement between predicted and measured hygroscopicity values. Their study represents an improvement in the hygroscopic treatment of organics over prior work, but is limited by both low time resolution and single-RH conditions inherent in HTDMA systems.

The current study presents data obtained during seven flights in the marine atmosphere off the coast of Central California during the second Marine Stratus/Stratocumulus Experiment (MASE-II). The dataset is the first to combine high-time-resolution, size-resolved AMS chemistry with high-time-resolution, size-resolved hygroscopic data at multiple RH values from the Differential Aerosol Sizing and Hygroscopicity Spectrometer Probe (DASH-SP). Hygroscopic studies have previously been carried out in the marine atmosphere (see Table 1), but none of those listed utilized either AMS chemical data or hygroscopic data as highly size-, time- and RH-resolved as those presented here.

2 Experimental

2.1 MASE-II Experiment

The data presented here were obtained during a series of seven cloud probing flights carried out as part of the second Marine Stratus/Stratocumulus Experiment (MASE-II) field campaign during July 2007. The MASE-II experiment was the second of two airborne field campaigns directed toward measurement of aerosol-cloud relationships in marine stratocumulus in the Eastern Pacific Ocean. The Marine Stratus/Stratocumulus Experiment (MASE) was carried out in 2005 off the coast of Monterey, California (Lu et al., 2007), and MASE-II was undertaken in 2007 in the same region. Both experiments were carried out in the month of July, when marine stratocumulus are prevalent over the region, and utilized the CIRPAS Twin Otter aircraft. In each campaign, comprehensive airborne measurements were made of aerosol and cloud properties in areas both perturbed and unperturbed by continental emissions. Tables 2 and 3 list the flights carried out during MASE-II and the instrument payload onboard the Twin Otter, respectively. The present study addresses measurements of the hygroscopic properties of marine aerosols during MASE-II. Other flights probed emissions from a large bovine source and a large container ship, and these data are presented elsewhere (Sorooshian et al., 2008b; Murphy et al., 2009).

2.2 Aerosol composition measurements

Non-refractory aerosol chemical species were characterized by the Aerodyne compact Time-of-Flight Aerosol Mass Spectrometer (C-ToF-AMS) (Drewnick et al., 2004a,b). Particles with vacuum aerodynamic diameters (D_{va}) 50 nm$\leq D_{va} \leq$800 nm are focused by an aerodynamic lens, pass through a 3.5% chopper, and are vaporized at 530–600°C. The chopper is operated in three modes, to detect background mass spectra, ensemble average mass spectra over all particle sizes, or size-resolved mass spectra. After particle vaporization, molecules are ionized via electron impact, and are pulsed into a time-of-flight mass spectrometer. MASE-II data were collected at unit mass resolution. AMS mass spectra are deconvolved into sulfate, nitrate, ammonium, and organic mass loadings (Allan et al., 2004). O:C ratios are determined by using mass concentration at m/z 44 and a parameterization presented in Aiken et al. (2008).

AMS measurements were averaged to match the time-resolution of hygroscopicity measurements, and particle density was calculated for each flight leg. Because the C-ToF-AMS measures particle vacuum aerodynamic diameter (D_{va}) and the DMA measures electrical mobility diameter (D_{em}), one can determine particle density by comparing the volume distribution from the DMA ($dV/d\log(D_{em})$) to the total mass distribution measured by the C-ToF-AMS ($dM/d\log(D_{va})$) (DeCarlo et al., 2004). If one assumes that the aerosol consists of an internal mixture of spherical particles, the relationship between the two diameters is $\rho_p=(D_{va}/D_{em})\rho_o$, where ρ_o is unit density (1 g/cm^3). Under these assumptions, the ratio of the D_{va} where the mass distribution peaks to the D_{em} where the volume distribution peaks is the density. Reference to the peak of each distribution is given for simplicity, though in practice the ratio that causes the entirety of the two distributions to best align is

Table 1. Previous marine aerosol hygroscopicity studies.

Investigators	Year	Study Area	Reported GFs
Hegg	1996	Eastern Pacific	1.4–2.0
Berg	1998	Pacific and Southern Oceans	1.56–1.78
Kotchenruther	1998	Mid-Atlantic	1.81–2.3*
Gasso	2000	Eastern Atlantic	γ=0.51 − 0.75**
Swietlicki	2000	Northeastern Atlantic	1.6–1.8
Zhou	2001	Arctic Ocean	1.4–1.9
Hegg	2002	Eastern Pacific	γ=0.2 − 0.7**
Vakeva	2002	Northeastern Atlantic	1.3–1.4***
Massling	2003	Atlantic and Indian Oceans	1.6–2.0
Hegg	2006	Eastern Pacific	1.3–1.5
Kaku	2006	Eastern Pacific	1.2–1.7
Tomlinson	2007	Southeastern Pacific	1.3–1.7****

* Ratio of light scattering coefficient at 80% RH to 30% RH.
** γ from the expression $b_{sp}(RH)/b_{sp}(RH_0) = ((1-RH/100)/(1-RH_0/100))^{-\gamma}$ (Kasten, 1969).
*** Aitken mode particles.
**** 85% RH.

Table 2. MASE-II flights.

Flight Number (RF)	Date (July 2007)	Type of Flight
1	10	Cloud/aerosol interactions
2	11	Cloud/aerosol interactions
3	12	Bovine source probe
4	14	Cloud/aerosol interactions
5	15	Cloud/aerosol interactions
6	16	Coordinated ship plume probe
7	21	Cloud/aerosol interactions
8	22	Cloud/aerosol interactions
9	23	Cloud/aerosol interactions
10	24	Cloud/aerosol interactions
11	25	Cloud/aerosol interactions
12	26	Cloud/aerosol interactions
13	28	Cloud/aerosol interactions
14	29	Cloud/aerosol interactions
15	30	Bovine source probe
16	31	Cloud/aerosol interactions

the final calculated particle density. Organic density is then calculated by using the bulk chemistry from the C-ToF-AMS for a given time period and assuming the particles measured by the DMA are completely dry. The dry densities of all the inorganic components are known and, assuming volume additivity, the density of the organic component can then be estimated. If the inorganic component of the particles measured by the DMA is not completely dry, this procedure will result in an underestimate of the particle density because the D_{em} will be larger than it would have been for a dry particle. Particles entering the C-ToF-AMS are assumed to be dry, and even if they are not completely devoid of water, the presence of small amounts of water causes little change in the vacuum aerodynamic diameter. One important issue concerning C-ToF-AMS data is the collection efficiency of particles within the instrument (Huffman et al., 2005). In this study, C-ToF-AMS mass loadings were confirmed by comparison between the sulfate measurements from the C-ToF-AMS and the Particle Into Liquid Sampler – Ion Chromatograph (PILS-IC, Brechtel Mfg. Inc.) during periods when there were no rapid fluctuations in particulate mass loading. Composition data represent size-resolved AMS chemistry averaged over 10 nm size bins.

2.3 Hygroscopicity measurements

Hygroscopicity measurements were carried out with the Differential Aerosol Sizing and Hygroscopicity Spectrometer Probe (DASH-SP, Brechtel Mfg; Sorooshian et al., 2008a). Ambient particles pass through a nafion dryer before receiving a uniform charge distribution in a ^{210}Po neutralizer. A cylindrical, single-classification differential mobility analyzer (DMA) then size selects particles into narrow ranges of mobility-equivalent diameters (D_{em}) between 0.1 and 1.0 μm. The resulting monodisperse aerosol is split into five separate flows. One channel provides a redundant measurement of total particle concentration at the DMA-selected size with a water condensation particle counter (TSI Model 3831). The remaining four channels consist of parallel nafion humidification chambers (Perma Pure, LLP, Model MD-070-24FS-4), followed by correspondingly humidified custom optical particle counters (OPCs). In the OPC sample volume, particles pass through a focused

Table 3. MASE-II instrument payload.

Parameter	Instrument	Time Resolution	Detection Limit	Size Range
Particle Number Concentration	Condensation Particle Counter (TSI CPC 3010)	1 s	0–10 000 cm^{-3}	$D_p \geq 10$ nm
Particle Number Concentration (including ultrafine)	Condensation Particle Counter (TSI CPC 3025)	1 s	0–100 000 cm^{-3}	$D_p \geq 3$ nm
Aerosol Size Distribution	Scanning differential mobility analyzer (Dual Automated Classified Aerosol Detector, DACAD)	73 s	N/A	10–700 nm
Aerosol Size Distribution	Passive Cavity Aerosol Spectrometer Probe (PCASP)	1 s	N/A	0.1–2.6 μm
Separation of Cloud Droplets From Interstitial Aerosol	Counterflow Virtual Impactor	N/A	N/A	N/A
Cloud Droplet Size Distribution	Phase Doppler Interferometer (PDI)	1 s	N/A	4–200 μm
Cloud and Drizzle Drop Size Distribution	Forward Scattering Spectrometer Probe (FSSP)	1 s	N/A	1–46 μm
Cloud Droplet Liquid Water Content	Light Diffraction (Gerber PVM-100 probe)	1 s	N/A	5–50 nm
Aerosol Bulk Ionic Composition and Soluble Organic Composition	Particle-Into-Liquid Sampler (PILS)	5 min	0.02–0.28 $\mu\mathrm{g/m}^3$	1 μm
Aerosol Bulk Composition (non-refractory species)	Aerodyne compact Time-of-Flight Aerosol Mass Spectrometer (C-ToF-AMS)	1 s or 15 s	$\leq$0.25 $\mathrm{g/m}^3$	40 nm$\leq D_{p,\,va} \leq$1 μm
Aerosol Hygroscopicity	Differential Aerosol Sizing and Hygroscopicity Spectrometer Probe (DASH-SP)	15–100 s	N/A	150 nm$\leq D_p \leq$1 μm
Soot Absorption	Photoacoustic Absoprtion Spectrometer (PAS)	1 s	1 Mm^{-1}	10 nm–5 μm
Soot Absorption	Particle Soot Absorption Photometer (PSAP)	$\geq$1 s	N/A	N/A

laser beam (λ=532 nm, World Star Technologies, Model TECGL-30) and scatter light in proportion to size (D_p) and refractive index (RI). Forward-scattered light is collected and focused on a photomultiplier tube, and the resulting electrical pulse is recorded by a high-speed data acquisition computer. An iterative data processing algorithm, based on laboratory calibrations with salts of known refractive indices, is used to determine the best fit on a solution surface relating electrical pulse height, size, and refractive index. The hygroscopic growth factor (GF=$D_{p,\,\mathrm{wet}}/D_{p,\,\mathrm{dry}}$) is corrected for the RI change caused by particulate liquid water at elevated RH. Temperature and pressure measurements are continually made at multiple locations in the instrument, and used to ensure that temperature and pressure variability do not impact hygroscopicity measurements.

In the current study, hygroscopicity was measured at dry sizes corresponding to D_{em} of 150, 175, and 200 nm. Multiple RH sensors in the nafion tubes and OPCs controlled RHs to dry ($\leq$8%), 74%, 85%, and 92%, with RH uncertainty of 1.5%. Low particle loadings inherent in the marine atmosphere required increased on-line collection times at each DMA size step, but usually $\leq$1 min was sufficient to overcome counting statistic limitations. Overall uncertainty in GF calculations is 4.5%.

Assuming particles to be uniform, non-light-absorbing spheres allows the assumption that the intensity of scattered light is a function of only RI and D_p. This assumption also allows calculation of dry, "effective" RI from the known DMA-selected D_p and measured scattered light intensity.

2.4 Hygroscopic closure

A volume-weighted mixing rule was used to perform a hygroscopic closure using AMS and DASH-SP data, under the assumption of independent and additive water uptake by individual constituents in each particle:

$$\mathrm{GF}_{\mathrm{mixed}}(a_w) = \left(\sum_i \epsilon_i \mathrm{GF}_i(a_w)^3\right)^{1/3} \tag{1}$$

where $\mathrm{GF}_{\mathrm{mixed}}$ is the overall particle GF, a_w is the water activity, GF_i is the hygroscopic growth factor for pure species i, and ϵ_i is the volume fraction of species i. At equilibrium, a_w=RH (Seinfeld and Pandis, 2006). Values for ϵ_i were calculated for the following species, using AMS masses of ammonium (NH_4^+), nitrate (NO_3^-), sulfate (SO_4^{2-}), and total organic: ammonium nitrate ($\mathrm{NH_4NO_3}$), ammonium sulfate ($\mathrm{(NH_4)_2SO_4}$), ammonium bisulfate ($\mathrm{NH_4HSO_4}$), sulfuric acid ($\mathrm{H_2SO_4}$), and organic. Partitioning between sulfate species was determined on the basis of the ammonium to sulfate molar ratio (SR=[NH_4^+]/SO_4^{2-}]). When SR≤1, the sulfate was assumed to be a mixture of H_2SO_4 and NH_4HSO_4; when 1<SR<2, sulfate was assumed to be a mixture of NH_4HSO_4 and $(NH_4)_2SO_4$; when SR≥2, sulfate was assumed to be solely $(NH_4)_2SO_4$. During MASE-II, sulfate was predominantly found to exist as NH_4HSO_4. $(NH_4)_2SO_4$ is assumed to have a GF of unity at RH equal to 74% since particles are exposed to RH well below its effloresence point before subsequent rehumidification. The organic fraction was assumed to be hydrophilic, based on evidence of a high degree of organic oxygenation from AMS mass spectra (see Sect. 3.3). Values of GF_i for the organic fraction were calculated as those necessary to minimize the root mean square error in comparing predictions with measured hygroscopicity.

3 Results

GF values for seven flights are presented (RF 7, 10, 11, 12, 13, 14, and 16 in Table 2). Table 4 presents measured GFs at each RH and each $D_{em,\,\mathrm{dry}}$. Typically, multiple measurements were made on each leg, at each size, for each flight. The error reported is ±one standard deviation in these multiple measurements. When only one measurement was made at a given size in a given leg, it is reported without error. Ship plumes were encountered on flights 10 and 16, as evidenced by brief, significantly elevated particle number concentration. Analysis of GF measurements in these presumptive plumes is not presented in the present work. Aerosol densities were calculated for each leg and used in the analysis below. Mission-averaged densities (averaged over all flight legs) were found to be 1.53±0.19, 1.56±0.20, and 1.47±0.15 g/cm^3 for below-cloud, above-cloud, and free troposphere legs, respectively. Mission-averaged organic densities were calculated to be 1.20±0.76, 1.34±0.46, and 1.30±0.24 for below-cloud, above-cloud, and free troposphere legs, respectively.

3.1 Airmass origin

Relative to the other flights, RF 12 and 16 exhibited significantly suppressed water uptake at high RH for all dry sizes. During these two flights, 92% GF values for 200 nm $D_{em,\,\mathrm{dry}}$ particles averaged 1.61±0.14, as compared with 1.91±0.07 for all other flights. These low-GF flights corresponded to significantly elevated total organic, as measured by the AMS. Mass concentration averaged 1.97±1.71 μg/m^3 organic (as opposed to 0.58±0.63 μg/m^3 for all other flights), corresponding to volume fraction organic (VF_{organic}) of 0.56±0.19 (as opposed to 0.39±0.20 for all other flights).

Back-trajectory analysis suggests that the MASE-II flights can be categorized by airmass origin as either polluted/continental (flights 12, 16), or non-continentally influenced (flights 7, 10, 11, 13, 14). Figure 1 shows 92% GF measurements for 200 nm $D_{em,\,\mathrm{dry}}$ particles, with corresponding 48-h HYSPLIT (available at: http://www.arl.noaa.gov/ready/hysplit4.html) back-trajectories identifying airmass origin. Note that the low GFs and high VF_{organic} measured on flights 12 and 16 correspond with airmass origins over the continental United States, while higher GFs and lower VF_{organic} measured on other flights correspond to airmass origins over the clean marine environment. It is interesting to note that trajectories at sea level have marine origins for all flights (including low-GF flights 12 and 16), and that there is a general trend of descending air from aloft over the course of the trajectories. This suggests that mixing of air from aloft is a significant factor in determining aerosol characteristics in the marine boundary layer. It is also noteworthy that GF values at low RH were not significantly suppressed, with values of 1.31±0.06 at 74% (compared with 1.31±0.07 for all other flights). GF values at intermediate RH were moderately suppressed in the continental airmasses, measuring 1.53±0.10 at 85% (compared with 1.58±0.08 for all other flights). In other words, the effect of the high-VF_{organic}, continental airmass was to significantly suppress GF at high RH, while having no measurable effect on aerosol water uptake at low RH and a moderate impact at intermediate RH. These results, while suggestive of continental airmass influence, should be interpreted in light of the relatively coarse grid resolution of the HYSPLIT model. In this analysis, small shifts in back-trajectories toward continental origin correlate with significantly suppressed high-RH GFs.

3.2 Hygroscopicity trends

No size-dependent hygroscopicity was observed over the range of measured $D_{em,\,\mathrm{dry}}$, and in addition, no significant size-dependent trends in VF_{organic} were observed. Further, organic-to-sulfate ratios from the AMS showed no significant variation over the size range measured by the DASH-SP. This suggests an internally-mixed aerosol between dry sizes of 150 and 200 nm.

Figure 2 shows below- and corresponding above-cloud 92% GF values for all flights. There exists a ubiquitous trend of higher below-cloud aerosol GF values at high RH when compared with top of cloud hygroscopicity values (1.88±0.14 below cloud, versus 1.78±0.18 above cloud). Marker sizes, proportional to VF_{organic}, suggest a trend of higher organic loading above cloud in several flights (0.36±0.15 below cloud, versus 0.43±0.22 above cloud). While variability is rather large in these measurements, the trend of elevated VF_{organic} above-cloud does correspond to suppressed GF at high RH. There is a trend of more moderate GF suppression at intermediate RH in the higher VF_{organic} above-cloud layer (1.53±0.06 above cloud, as compared with 1.58±0.07 below cloud). Unlike the continental-influenced flights, there is evidence of greater suppression of low-RH GFs in above-cloud legs, with 74% GF values of

1.31±0.05 above cloud, compared with 1.36±0.05 below. It appears, then, that the elevated organic loadings typical of above-cloud legs are correlated with GF suppression at high RH, and more moderate GF suppression at lower RHs.

3.3 Hygroscopic closure

A hygroscopic closure was performed, using volume-weighted hygroscopic contributions from each chemical constituent identified by the AMS. O:C ratios for the flights presented were very similar for below-cloud (0.93±0.32), above-cloud (0.91±0.26), and free troposphere (0.92±0.25) legs in both continentally- (0.94±0.30) and marine-influenced (0.91±0.25) flights. This result indicates that the organic component was consistently highly oxidized. With this evidence, the organic fraction was treated as a bulk, water-soluble constituent and was not divided into soluble and insoluble fractions based on AMS organic mass spectra (Kondo et al., 2007). As described in Sect. 2.4, GF values were calculated for the organic component of the aerosol by minimizing root mean square error when comparing measured GFs with volume-weighted closure predictions. Mission-averaged organic GFs were determined to be 1.22, 1.45, and 1.48 at 74, 85, and 92% RH, respectively. Agreement at 74 and 92% RH is within 2%, compared with the hydrophilic multifunctional and dicarboxylic acids parameterized in Peng et al. 2001, though the 85% organic GF is overpredicted here by 7%. Closure results are presented in Fig. 3. Markers in Fig. 3 are color-coded according to relative humidity, and marker size is proportional to $\mathrm{VF}_{\mathrm{organic}}$. The volume-weighted hygroscopic closure utilizing size-resolved AMS chemistry achieves good agreement with the 675 DASH-SP GF measurements, with an R^2 of 0.78. Agreement is better at lower values of RH, owing to smaller GF magnitudes and less overall GF variability.

Aside from the obvious RH dependence of GF values, the clearest trend in Fig. 3 is that of larger markers (higher $\mathrm{VF}_{\mathrm{organic}}$) at low GF transitioning to smaller markers (lower $\mathrm{VF}_{\mathrm{organic}}$) at high values of GF for the same RH. The clarity and regularity of this trend reveal the importance of the organic fraction in determining GF values.

3.4 Simplified parameterization

To further investigate the relative importance of each parameter in quantifying aerosol water uptake, and to detemine the simplest empirical model still capable of accurately predicting GF, a backward stepwise linear regression was performed. The process, which eliminates predictors one-by-one to generate increasingly simplified linear representations of data, started with over 60 predictors, ranging from PILS and AMS chemical parameters to atmospheric data. The result is a two-parameter model that predicts GF as a function of RH and $\mathrm{VF}_{\mathrm{organic}}$:

$$\mathrm{GF} = -0.312 + 0.0233(\mathrm{RH}) - 0.282(\mathrm{VF}_{\mathrm{organic}}) \qquad (2)$$

Figure 4 demonstrates the accuracy with which this model predicts DASH-SP GF values over the measured the range of RH and $\mathrm{VF}_{\mathrm{organic}}$. It is noteworthy that the R^2 for this model is 0.77, indicating that the simple, two-parameter model explains only 1% less variability than the full volume-weighted chemical closure, which contains significantly more information (i.e. multiple inorganic chemical species and their individual GFs, in addition to organic fraction with its associated GF). It appears as though accurate predictions of particle water uptake in this region can be made simply on the basis of relative humidity and the relative abundance of organics in the aerosol, given a relatively uniform, highly-oxidized organic component internally mixed with predominantly ammonium bisulfate. While this model accurately predicts GF over the range of RH and $\mathrm{VF}_{\mathrm{organic}}$, and for the O:C ratios measured during MASE-II, it should not be used when RH is outside the range $74\% \leq \mathrm{RH} \leq 92\%$, or where $\mathrm{VF}_{\mathrm{organic}}$ is less than 0.1 or greater than 0.9.

4 Discussion

Comparing mixed organic-inorganic particles with those comprised entirely of inorganic salts, there is a strong RH-dependence in the effect of organics on hygroscopicity (Peng et al., 2001). During the MASE-II field campaign, GF values at 74% RH averaged ~1.3. Organic GFs were calculated to be 1.22 at 74% RH, suggesting that they contributed significantly to overall aerosol water uptake at low RH. GF values at 85% RH averaged ~1.6 during the campaign, and so the organic GF of 1.45 calculated for 85% RH suggests that organics played a less significant role, but still influenced water uptake at intermediate RH. An organic GF value of 1.48 was calculated for 92% RH, with DASH-SP 92% GF measurements of ~1.8 indicating that organics make little contribution to overall water uptake at high RH.

Inorganic salts exhibit deliquescent behavior as RH is increased. Many organics do not deliquesce or crystallize when RH is increased or decreased, respectively, but instead retain water at RH values well below the RH of deliquescence (RHD) of the inorganic salts with which they often co-exist in ambient particles. As a result, at RH values below the salt RHD, the presence of organics enhances water uptake. Thus, the effect of organics is to contribute significantly to overall water uptake at low values of RH in mixed organic-inorganic particles. At high RH, on the other hand, organics tend to take up significantly less water than the inorganic constituents with which they co-exist in ambient particles. Therefore, at RH values above the inorganic RHD, organics appear to suppress water uptake relative to that which a pure inorganic particle would exhibit.

Figure 5 shows simplified behavior of a pure ammonium sulfate (AS) particle, pure organic acid (OA) particle (as described by Peng et al., 2001), and a mixed organic acid and ammonium sulfate (OA/AS) particle over the range

Table 4. GF results for below, above, free troposphere (FT), and ship plume measurements.

150 nm												
Flight	Below			Above			FT			Ship Plume		
	74%	85%	92%	74%	85%	92%	74%	85%	92%	74%	85%	92%
7	1.40±0.04	1.57±0.03	1.82±0.05	1.26±0.06	1.55±0.04	1.78±0.01	1.40±0.03	1.55±0.03	1.84±0.04			
10	1.42±0.04	1.60±0.06	1.80±0.04	1.37±0.10	1.57±0.04	1.71±0.11	1.42±0.03	1.56±0.04	1.70±0.07	1.42±0.04	1.62±0.03	1.78±0.04
11	1.44±0.05	1.61±0.06	1.80±0.07	1.40±0.07	1.51±0.02	1.64±0.05	1.38±0.07	1.52±0.06	1.65±0.10			
12	1.38±0.03	1.58±0.03	1.63±0.04	1.34±0.04	1.51±0.03	1.55±0.01	1.38±0.02	1.60±0.01	1.63±0.01			
13	1.39±0.01	1.61±0.05	1.82±0.02	1.35±0.01	1.61±0.03	1.75±0.05	1.27±0.05	1.49±0.07	1.61±0.08			
14	1.36±0.05	1.65±0.21	1.82±0.14	1.39±0.02	1.62±0.01	1.87±0.09	1.37±0.03	1.60±0.03	1.77±0.06			
16	1.41±0.02	1.58±0.05	1.64±0.08	1.33±0.03	1.52±0.03	1.54±0.03	1.29±0.04	1.49±0.07	1.52±0.06	1.38±0.02	1.59±0.02	1.61±0.04

175 nm												
Flight	Below			Above			FT			Ship Plume		
	74%	85%	92%	74%	85%	92%	74%	85%	92%	74%	85%	92%
7	1.36±0.06	1.54±0.02	1.95±0.03	1.28±0.04	1.53±0.03	1.91±0.06	1.24±0.08	1.52±0.03	1.87±0.10			
10	1.41±0.06	1.59±0.05	1.93±0.02	1.34±0.05	1.51±0.01	1.83±0.06	1.33±0.02	1.60±0.03	1.89±0.05	1.34±0.02	1.55±0.05	1.88±0.06
11	1.31±0.08	1.48±0.07	1.82±0.09	1.31±0.03	1.44±0.09	1.77±0.03	1.33±0.04	1.53±0.12	1.77±0.23			
12	1.33±0.02	1.55±0.04	1.63±0.08	1.26±0.06	1.48±0.08	1.51±0.07	1.35±0.02	1.57±0.01	1.60±0.01			
13	1.34±0.03	1.58±0.04	2.00±0.05	1.3	1.55	1.78	1.24±0.05	1.44±0.06	1.63±0.10			
14	1.34±0.01	1.63±0.02	2.03±0.01	1.32±0.02	1.58±0.02	1.91±0.05	1.33±0.02	1.50±0.08	1.79±0.22			
16	1.35±0.04	1.54±0.03	1.62±0.06	1.28±0.02	1.43±0.04	1.45±0.04	1.24±0.04	1.38±0.06	1.40±0.10	1.33±0.03	1.52±0.04	1.55±0.03

200 nm												
Flight	Below			Above			FT			Ship Plume		
	74%	85%	92%	74%	85%	92%	74%	85%	92%	74%	85%	92%
7	1.37±0.04	1.57±0.03	1.98±0.03	1.22±0.06	1.56±0.05	1.92±0.01	1.21±0.01	1.54±0.08	1.91±0.04			
10	1.41±0.09	1.72±0.09	2.01±0.05	1.33±0.02	1.57±0.07	1.87±0.04	1.35±0.01	1.63±0.06	1.93±0.06	1.33±0.04	1.66±0.06	1.95±0.05
11	1.25±0.11	1.45±0.17	1.86±0.07	1.26	1.47	1.83	1.36±0.16	1.56±0.15	1.89±0.20			
12	1.33±0.03	1.64±0.03	1.73±0.05	1.29±0.03	1.48±0.10	1.55±0.12	1.37±0.05	1.64±0.05	1.69±0.04			
13	1.36±0.05	1.68±0.05	2.01±0.04	1.3	1.61	1.85	1.21±0.08	1.45±0.07	1.78±0.12			
14	1.42±0.11	1.65±0.05	1.98±0.10	1.31±0.05	1.60±0.03	1.96±0.01	1.35±0.09	1.59±0.10	1.89±0.11			
16	1.35±0.02	1.59±0.05	1.77±0.08	1.26±0.02	1.45±0.08	1.53±0.10	1.23±0.06	1.40±0.10	1.40±0.11	1.33±0.03	1.62±0.04	1.66±0.06

50%≤RH≤94%. Note that the mixed OA/AS particle shows smooth growth with RH, as opposed to the deliquescent behavior exhibited by the pure AS particle. The tendency of organics to retain water at low RH causes water uptake behavior for the OA/AS particle to follow that of the descending (i.e. efflorescence) branch of the pure AS growth curve. Since pure OA takes up less water at high RH than does pure AS, the growth curve for the OA/AS particle is suppressed, compared with that of pure AS. The overall result, as predicted by thermodynamic theory, is that the presence of OA leads to enhanced water uptake at low RH and suppressed GF at high RH.

Virkkula et al. (1999) concluded that the most important factor contributing to GF suppression at high RH was the volume fraction of organic present in an aerosol. Others have suggested that the exact chemical identity of the organic constituents is not especially important, and that for an organic component classified as either oxidized or hydrocarbon-like, its relative abundance determines its effect on GF values (McFiggans et al., 2005; Moore and Raymond, 2008). The aerosol measured during MASE-II was comprised of an internally-mixed combination of highly-oxidized organics with predominantly ammonium bisulfate in the size range 150–200 nm. Results presented here from a stepwise linear regression on GF data from the marine atmosphere suggest that the single most important factor in predicting GF (aside from RH) is, indeed, $\mathrm{VF}_{\mathrm{organic}}$. This suggests that an aerosol containing a uniform, highly-oxidized organic component may be sufficiently characterized in global models by a size distribution, RH, and a bulk estimate of the relative abundance of organics.

A brief sensitivity study was undertaken, in order to determine the importance of the $\mathrm{VF}_{\mathrm{organic}}$ term in predicting water uptake for the marine aerosol encountered during this study. Predictions of hygroscopic GF based on the assumption of an entirely inorganic aerosol yielded poorer agreement (R^2=0.68) than the simple parameterization presented in this paper (R^2=0.77). This suggests that accurate predictions of organic volume fraction are important to predict water uptake for a marine aerosol with a uniformly oxidized organic component.

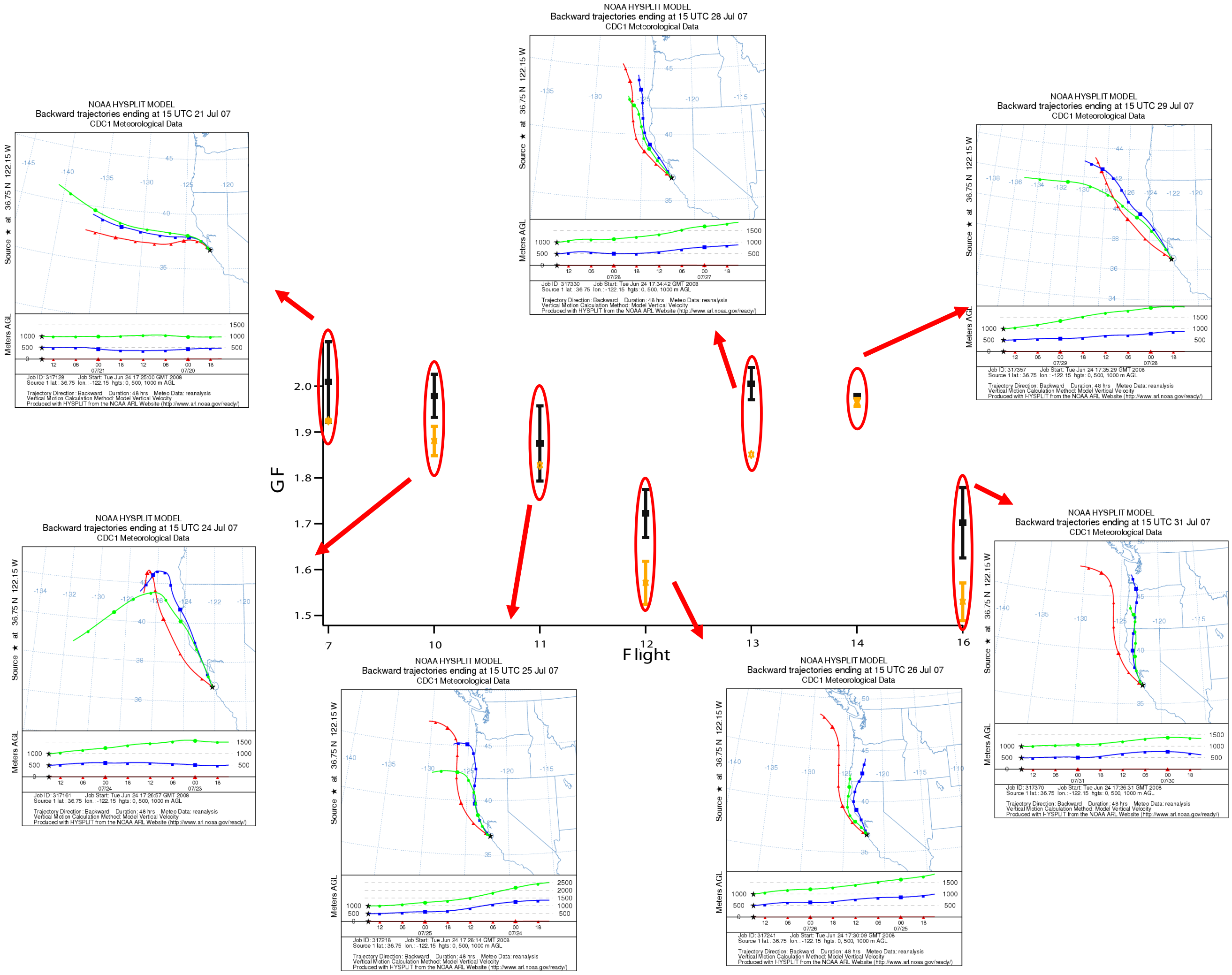

Fig. 1. 92% GF values for $D_{em,\,\mathrm{dry}}$=200 nm particles are shown for below (black) and above (yellow) cloud flight legs. 48-h HYSPLIT back-trajectories show airmass origin for each flight. Flights 12 and 16 show both suppressed GF values and continental, polluted airmass origin.

In most instruments that measure aerosol hygroscopicity, residence times for humidification are on the order of seconds; much longer than the equilibration time for most inorganics with water vapor. Sjogren et al. (2007) noted, however, that particles with high volume fraction organic material may require as long as 40 s to achieve equilibrium with water vapor. If such long times are necessary to achieve equilibrium, hygroscopic measurement methods suitable for the field will tend to overpredict GF at low RH (water vapor does not evaporate completely from the particle during the drying process), while underpredicting GF at high RH (insufficient humidification time is provided for the organic fraction to achieve thermodynamic equilibrium with water vapor). In electrodynamic balance (EDB, Cohen et al., 1987a,b,c) studies, suspended particles are subjected to extended exposure to water vapor (minutes to hours), establishing equilibrium. Some organics exhibit extremely high deliquescence relative humidities (DRH) (e.g., oxalic acid), while others exhibit gradual hygroscopic growth at low RH and substantial growth at high RH (e.g., malonic acid) (Peng et al., 2001). It is possible, given the wide range of organic species in the atmosphere and correspondingly wide range of hygroscopic properties associated with those species, and the relatively short humidification times in the DASH-SP and other similar instruments, that the effects attributed to organics may reflect some kinetic instrumental limitations.

Additionally, while particles entering the DASH-SP are dried to well below relative humidity of efflorescence (RHE) for the inorganic salts encountered in the marine atmosphere, it is possible that the presence of organics causes some particles to remain in a supersaturated (with respect to efflorescence) state after drying. The inorganic fraction of such

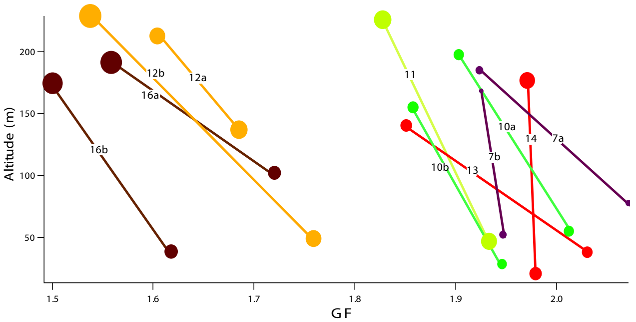

Fig. 2. Below- and above-cloud 92% GF values for $D_{em, dry}$ 200vnm particles as a function of altitude, with lines connecting measurements made on the same 'trip' from bottom to top of cloud. Marker size is proportional to $VF_{organic}$, and ranges from 0.10 to 0.90. "a" and "b" designate separate "trips" during the same flight.

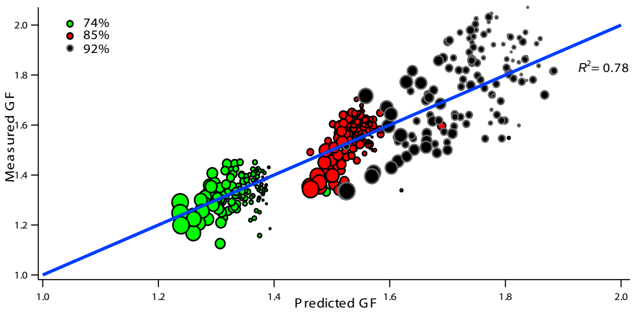

Fig. 3. Measured GF values versus volume-weighted predictions. Markers are color-coded with RH, and marker size is proportional to $VF_{organic}$ (ranging from 0.10 to 0.90). The blue line represents 1:1.

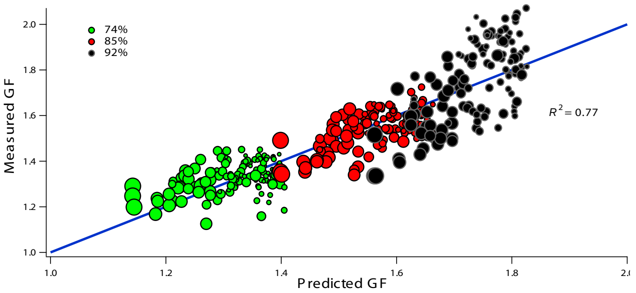

Fig. 4. Predictions of GF from the simplified parameterization. Markers are color-coded with RH, and marker size is proportional to $VF_{organic}$ (ranging from 0.10 to 0.90). The blue line represents 1:1.

a supersaturated particle would exhibit gradual water uptake with increased relative humidity, even at RH lower than the RHD for the inorganic salt. Assuming deliquescent behavior of the inorganic salt (i.e. the inorganic fraction is crystalline at RH RHE), this enhanced water uptake at low RH would be attributed to solely the organic fraction, thereby leading to a potential overestimation in the organic GF.

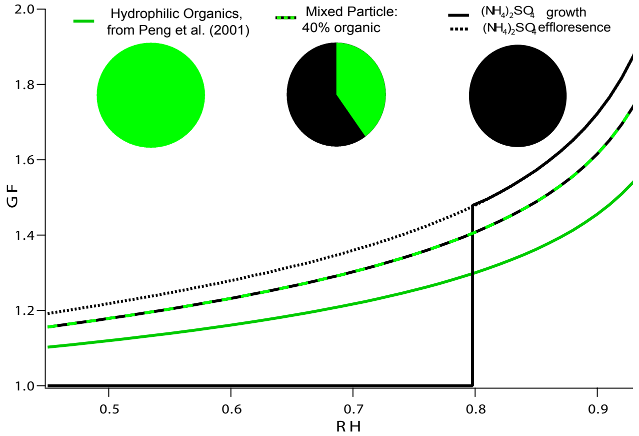

Fig. 5. Comparison of growth curves for pure ammonium sulfate, pure hydrophilic organic, and mixed organic/inorganic particles. Ammonium sulfate curves calculated from AIM (Clegg et al., 1998).

5 Conclusions

We report a hygroscopic closure study for the coastal California aerosol, using size-resolved C-ToF-AMS chemical data coupled with highly time-resolved, multiple-RH hygroscopicity measurements from the DASH-SP.

Airmasses originating from continental locations showed elevated organic loading, and correspond to significant GF suppression at high RH. More moderate GF suppression was measured at intermediate RH and no impact was observed at low RH. A comparison of above-cloud with below-cloud aerosol indicated that a slightly organic-enriched layer above cloud corresponded with suppressed GFs at high RH. A volume-weighted hygroscopic closure provided excellent agreement with measured GFs, and mission-averaged organic GFs at 74, 85, and 92% were calculated to be 1.22, 1.45, and 1.48, respectively. These GF values are relatively high when compared with many previous estimations of organic GF, but agree well with values reported for dicarboxylic and multifunctional acids. These high organic GFs are indicative of the highly oxidized state of the aged organic fraction. A simplified parameterization for predicting GF was developed using a stepwise linear regression method. This parameterization is a function of only RH and $VF_{organic}$, and explains only 1% less variability than does the volume-weighted chemical closure. These results may be more broadly applicable to similar coastal conditions, where some aged organics are present in an otherwise marine-influenced atmosphere.

The richness of this hygroscopic/chemical data set underlies the significance of coupling the DASH-SP instrument with the AMS. The improved time resolution available with the DASH-SP eliminates much of the time-averaging of AMS composition data that is otherwise necessary with less highly time-resolved HTDMA hygroscopicity measurements. The importance of simultaneous GF measurements at multiple RH values is demonstrated by a simplified parameterization for predicting GF as a function of RH and $\mathrm{VF}_{\mathrm{organic}}$; a result potentially important for efficiently representing aerosol-water interactions in global models.

Acknowledgements. This work was supported by the Office of Naval Research grant N00014-04-1-0118. We acknowledge the committed, meticulous work of the CIRPAS Twin Otter crew, especially pilot Mike Hubbell and copilot Chris McGuire.

Edited by: A. Nenes

References

Aiken, A. C., DeCarlo, P. F., Kroll, J., Worsnop, D., J.A., H., Docherty, K., Ulbrich, I., Mohr, C., Kimmel, J., Sueper, D., Sun, Y., Zhang, Q., Trimborn, A., Northway, M., Ziemann, P., Canagaratna, M., Onsach, T., Alfarra, M., Prevot, A., Dommen, J., Duplissy, J., Metzger, A., Baltensperger, U., and Jimenez, J. L.: O/C and OM/OC Ratios of Primary, Secondary, and Ambient Organic Aerosols with High-Resolution Time-of-Flight Aerosol Mass Spectrometry, Environ. Sci. Technol., 42, 4478–4485, 2008.

Allan, J., Bower, K., Alfarra, M., Delia, A., Jimenez, J., Middlebrook, A., Drewnick, F., Onasch, T., Canagaratna, M., Jayne, J., and Worsnop, D.: Technical note: Extraction of Chemically Resolved Mass Spectra from Aerodyne Aerosol Mass Spectrometer Data, J. Aerosol Sci., 35, 909–922, 2004.

Ansari, A. S. and Pandis, S. N.: Water absorption by secondary organic aerosol and its effect an inorganic aerosol behavior, Environ. Sci. Technol., 34, 71–77, 2000.

Berg, O. H., Swietlicki, E., and Krejci, R.: Hygroscopic growth of aerosol particles in the marine boundary layer over the Pacific and Southern Oceans during the First Aerosol Characterization Experiment (ACE 1), J. Geophys. Res., 103, 16 535–16 545, 1998.

Carrico, C. M., Rood, M. J., and Ogren, J. A.: Aerosol light scattering properties at Cape Grim, Tasmania, during the First Aerosol Characterization Experiment (ACE 1), J. Geophys. Res., 103, 16 565–16 574, 1998.

Carrico, C. M., Rood, M. J., Ogren, J. A., Neususs, C., Wiedensohler, A., and Heintzenberg, J.: Aerosol optical properties at Sagres, Portugal during ACE-2, Tellus B, 52, 694–715, 2000.

Choi, M. Y. and Chan, C. K.: Continuous measurements of the water activities of aqueous droplets of water-soluble organic compounds, J. Phys. Chem. A, 106, 4566–4572, 2002a.

Choi, M. Y. and Chan, C. K.: The effects of organic species on the hygroscopic behaviors of inorganic aerosols, Environ. Sci. Technol., 36, 2422–2428, 2002b.

Clegg, S. L. and Seinfeld, J. H.: Thermodynamic models of aqueous solutions containing inorganic electrolytes and dicarboxylic acids at 298.15 K. 2. Systems including dissociation equilibria, J. Phys. Chem. A, 110, 5718–5734, 2006.

Clegg, S. L., Brimblecombe, P., and Wexler, A. S.: Thermodynamic model of the system $\mathrm{H}^+-\mathrm{NH}_4^+-\mathrm{SO}_4^{2-}-\mathrm{NO}_3^--\mathrm{H}_2\mathrm{O}$ at tropospheric temperatures, J. Phys. Chem. A, 102(12), 2137–2154, 1998.

Cocker, D. R., Clegg, S. L., Flagan, R. C., and Seinfeld, J. H.: The effect of water on gas-particle partitioning of secondary organic aerosol. Part I: alpha-pinene/ozone system, Atmos. Environ., 35, 6049–6072, 2001a.

Cocker, D. R., Mader, B. T., Kalberer, M., Flagan, R. C., and Seinfeld, J. H.: The effect of water on gas-particle partitioning of secondary organic aerosol: II. m-xylene and 1,3,5-trimethylbenzene photooxidation systems, Atmos. Environ., 35, 6073–6085, 2001b.

Cohen, M. D., Flagan, R. C., and Seinfeld, J. H.: Studies of concentrated electrolyte-solutions using the electrodynamic balance. 1. Water activities for single-electrolyte solutions, J. Phys. Chem., 91, 4563–4574, 1987a.

Cohen, M. D., Flagan, R. C., and Seinfeld, J. H.: Studies of concentrated electrolyte-solutions using the electrodynamic balance. 2. Water activities for mixed-electrolyte solutions, J. Phys. Chem., 91, 4575–4582, 1987b.

Cohen, M. D., Flagan, R. C., and Seinfeld, J. H.: Studies of concentrated electrolyte-solutions using the electrodynamic balance. 3. Solute nucleation, J. Phys. Chem., 91, 4583–4590, 1987c.

Cruz, C. N. and Pandis, S. N.: Deliquescence and hygroscopic growth of mixed inorganic-organic atmospheric aerosol, Environ. Sci. Technol., 34, 4313–4319, 2000.

DeCarlo, P., Slowik, J., Worsnop, D., Davidovits, P., and Jimenez, J.: Particle Morphology and Density Characterization by Combined Mobility and Aerodynamic Diameter Measurements. Part 1: Theory, Aerosol. Sci. Tech., 39, 1185–1205, 2004.

Dougle, P. G., Veefkind, J. P., and ten Brink, H. M.: Crystallisation of mixtures of ammonium nitrate, ammonium sulphate and soot, J. Aerosol Sci., 29, 375–386, 1998.

Drewnick, F., Jayne, J. T., Canagaratna, M., Worsnop, D. R., and Demerjian, K. L.: Measurement of ambient aerosol composition during the PMTACS-NY 2001 using an aerosol mass spectrometer. Part II: Chemically speciated mass distributions, Aerosol. Sci. Tech., 38, 104–117, suppl. 1, 2004a.

Drewnick, F., Schwab, J. J., Jayne, J. T., Canagaratna, M., Worsnop, D. R., and Demerjian, K. L.: Measurement of ambient aerosol composition during the PMTACS-NY 2001 using an aerosol mass spectrometer. Part I: Mass concentrations, Aerosol. Sci. Tech., 38, 92–103, suppl. 1, 2004b.

Duplissy, J., Gysel, M., Alfarra, M. R., Dommen, J., Metzger, A., Prevot, A. S. H., Weingartner, E., Laaksonen, A., Raatikainen, T., Good, N., Turner, S. F., McFiggans, G., and Baltensperger, U.: Cloud forming potential of secondary organic aerosol under near atmospheric conditions, Geophys. Res. Lett., 35, L03818, doi:10.1029/2007GL031075, 2008.

Gasso, S., Hegg, D. A., Covert, D. S., Collins, D., Noone, K. J., Ostrom, E., Schmid, B., Russell, P. B., Livingston, J. M., Durkee, P. A., and Jonsson, H.: Influence of humidity on the aerosol scattering coefficient and its effect on the upwelling radiance during ACE-2, Tellus B, 52(2), 546–567, 2000.

Gysel, M., Crosier, J., Topping, D. O., Whitehead, J. D., Bower, K. N., Cubison, M. J., Williams, P. I., Flynn, M. J., McFiggans, G. B., and Coe, H.: Closure study between chemical composition and hygroscopic growth of aerosol particles during TORCH2, Atmos. Chem. Phys., 7, 6131–6144, 2007, http://www.atmos-chem-phys.net/7/6131/2007/.

Hameri, K., Charlson, R., and Hansson, H. C.: Hygroscopic properties of mixed ammonium sulfate and carboxylic acids particles, AIChE J., 48, 1309–1316, 2002.

Hegg, D. A., Covert, D. S., Rood, M. J., and Hobbs, P. V.: Measurements of aerosol optical properties in marine air, J. Geophys. Res., 101, 12 893–12 903, 1996.

Hegg, D. A., Covert, D. S., Crahan, K., and Jonssen, H.: The dependence of aerosol light-scattering on RH over the Pacific Ocean, Geophys. Res. Lett., 29, 60–4, 2002.

Hegg, D. A., Covert, D. S., Crahan, K. K., Jonsson, H. H., and Liu, Y.: Measurements of aerosol size-resolved hygroscopicity at sub and supermicron sizes, Geophys. Res. Lett., 33, L21808, doi:10.1029/2006GL026747, 2006.

Huffman, J., Jayne, J., Drewnick, F., Aiken, A., Onasch, T., Worsnop, D., and Jimenez, J.: Design, modeling, optimization, and experimental tests of a particle beam width probe for the aerodyne aerosol mass spectrometer, J. Aerosol Sci., 38, 1143–1163, 2005.

IPCC: Climate Change 2007: The Physical Science Basis. Contribution of Working Group I to the Fourth Assessment Report of the Intergovernmental Panel on Climate Change, Cambridge University Press, Cambridge, United Kingdom and New York, NY, USA, 153–180, 2007.

Kaku, K. C., Hegg, D. A., Covert, D. S., Santarpia, J. L., Jonsson, H., Buzorius, G., and Collins, D. R.: Organics in the Northeastern Pacific and their impacts on aerosol hygroscopicity in the subsaturated and supersaturated regimes, Atmos. Chem. Phys., 6, 4101–4115, 2006, http://www.atmos-chem-phys.net/6/4101/2006/.

Kasten, F.: Visibility forecast in phase of pre-condensation, Tellus, 21(5), 631–635, 1969.

Kim, J., Yoon, S. C., Jefferson, A., and Kim, S. W.: Aerosol hygroscopic properties during Asian dust, pollution, and biomass burning episodes at Gosan, Korea in April 2001, Atmos. Environ., 40, 1550–1560, 2006.

Kondo, Y., Miyazaki, Y., Takegawa, N., Miyakawa, T., Weber, R. J., Jimenez, J. L., Zhang, Q., and Worsnop, D. R.: Oxygenated and water-soluble organic aerosols in Tokyo, J. Geophys. Res., 112, D01203, doi:10.1029/2006JD007056, 2007.

Kreisberg, N. M., Stolzenburg, M. R., Hering, S. V., Dick, W. D., and McMurry, P. H.: A new method for measuring the dependence of particle size distributions on relative humidity, with application to the Southeastern Aerosol and Visibility Study, J. Geophys. Res., 106, 14 935–14 949, 2001.

Lu, M. L., Conant, W. C., Jonsson, H. H., Varutbangkul, V., Flagan, R. C., and Seinfeld, J. H.: The Marine Stratus/Stratocumulus Experiment (MASE): Aerosol-cloud relationships in marine stratocumulus, J. Geophys. Res., 112, D10209, doi:10.1029/2006JD007985, 2007.

Magi, B. I. and Hobbs, P. V.: Effects of humidity on aerosols in southern Africa during the biomass burning season, J. Geophys. Res., 108, 8495, doi:10.1029/2002JD002144, 2003.

Malm, W. C., Day, D. E., Kreidenweis, S. M., Collett, J. L., Carrico, C., McMeeking, G., and Lee, T.: Hygroscopic properties of an organic-laden aerosol, Atmos. Environ., 39, 4969–4982, 2005.

Massling, A., Leinert, S., Wiedensohler, A., and Covert, D.: Hygroscopic growth of sub-micrometer and one-micrometer aerosol particles measured during ACE-Asia, Atmos. Chem. Phys., 7, 3249–3259, 2007, http://www.atmos-chem-phys.net/7/3249/2007/.

Massling, A., Wiedensohler, A., Busch, B., Neusüß, C., Quinn, P., Bates, T., and Covert, D.: Hygroscopic properties of different aerosol types over the Atlantic and Indian Oceans, Atmos. Chem. Phys., 3, 1377–1397, 2003, http://www.atmos-chem-phys.net/3/1377/2003/.

McFiggans, G., Alfarra, M. R., Allan, J., Bower, K., Coe, H., Cubison, M., Topping, D., Williams, P., Decesari, S., Facchini, C., and Fuzzi, S.: Simplification of the representation of the organic component of atmospheric particulates, Faraday Discuss., 130, 341–362, 2005.

Moore, R. H. and Raymond, T. M.: HTDMA analysis of multicomponent dicarboxylic acid aerosols with comparison to UNIFAC and ZSR, J. Geophys. Res., 113, D04206, doi:10.1029/2007JD008660, 2008.

Murphy, S., Agrawal, H., Sorooshian, A., Padaro, L., Gates, H., Hersey, S., Welch, W., Jung, H., Miller, J., Cocker, D., Nenes, A., Jonsson, H., Flagan, R., and Seinfeld, J.: Comprehensive Simultaneous Shipboard and Airborne Characterization of Exhaust from a Modern Container Ship at Sea, Environmen. Sci. Technol., doi:10.1021/es802413j, published online: http://pubs.acs.org/doi/abs/10.1021/es802413j, 2009

Peng, C., Chan, M. N., and Chan, C. K.: The hygroscopic properties of dicarboxylic and multifunctional acids: Measurements and UNIFAC predictions, Environ. Sci. Technol., 35, 4495–4501, 2001.

Peng, C. G. and Chan, C. K.: The water cycles of water-soluble organic salts of atmospheric importance, Atmos. Environ., 35, 1183–1192, 2001.

Petters, M. D., Kreidenweis, S. M., Snider, J. R., Koehler, K. A., Wang, Q., Prenni, A. J., and Demott, P. J.: Cloud droplet activation of polymerized organic aerosol, Tellus B, 58, 196–205, 2006.

Prenni, A. J., DeMott, P. J., Kreidenweis, S. M., Sherman, D. E., Russell, L. M., and Ming, Y.: The effects of low molecular weight dicarboxylic acids on cloud formation, J. Phys. Chem. A, 105, 11 240–11 248, 2001.

Prenni, A. J., De Mott, P. J., and Kreidenweis, S. M.: Water uptake of internally mixed particles containing ammonium sulfate and dicarboxylic acids, Atmos. Environ., 37, 4243–4251, 2003.

Prenni, A. J., Petters, M. D., Kreidenweis, S. M., DeMott, P. J., and Ziemann, P. J.: Cloud droplet activation of secondary organic aerosol, J. Geophys. Res., 112, D10223, doi:10.1029/2006JD007963, 2007.

Rood, M. J., Larson, T. V., Covert, D. S., and Ahlquist, N. C.: Measurement of laboratory and ambient aerosols with temperature and humidity controlled nephlometry, Atmos. Environ., 19, 1181–1190, 1985.

Saathoff, H., Naumann, K. H., Schnaiter, M., Schock, W., Mohler, O., Schurath, U., Weingartner, E., Gysel, M., and Baltensperger, U.: Coating of soot and $(NH_4)_2SO_4$ particles by ozonolysis products of alpha-pinene, J. Aerosol Sci., 34, 1297–1321, 2003.

Seinfeld, J. and Pandis, S.: Atmospheric Chemistry and Physics, Wiley-Interscience, New York, NY, USA, 2nd edn., 2006.

Sjogren, S., Gysel, M., Weingartner, E., Baltensperger, U., Cubison, M. J., Coe, H., Zardini, A. A., Marcolli, C., Krieger, U. K., and Peter, T.: Hygroscopic growth and water uptake kinetics of two-phase aerosol particles consisting of ammonium sulfate, adipic and humic acid mixtures, J. Aerosol Sci., 38, 157–171, 2007.

Sorooshian, A., Hersey, S., Brechtel, F., Corless, A., Flagan, R., and Seinfeld, J.: Rapid, Size-Resolved Aerosol Hygroscopic Growth Measurements: Differential Aerosol Sizing and Hygroscopicity Spectrometer Probe (DASH-SP), Aerosol. Sci. Tech., 42, 445–464, 2008a.

Sorooshian, A., Murphy, S. M., Hersey, S., Gates, H., Padro, L. T., Nenes, A., Brechtel, F. J., Jonsson, H., Flagan, R. C., and Seinfeld, J. H.: Comprehensive airborne characterization of aerosol from a major bovine source, Atmos. Chem. Phys., 8, 5489–5520, 2008b.

Swietlicki, E., Zhou, J. C., Covert, D. S., Hameri, K., Busch, B., Vakeva, M., Dusek, U., Berg, O. H., Wiedensohler, A., Aalto, P., Makela, J., Martinsson, B. G., Papaspiropoulos, G., Mentes, B., Frank, G., and Stratmann, F.: Hygroscopic properties of aerosol particles in the northeastern Atlantic during ACE-2, Tellus B, 52, 201–227, 2000.

Tomlinson, J. M., Li, R. J., and Collins, D. R.: Physical and chemical properties of the aerosol within the southeastern Pacific marine boundary layer, J. Geophys. Res., 112, 1–13, 2007.

Topping, D. O., McFiggans, G. B., and Coe, H.: A curved multicomponent aerosol hygroscopicity model framework: Part 1 - Inorganic compounds, Atmos. Chem. Phys., 5, 1205–1222, 2005a.

Topping, D. O., McFiggans, G. B., and Coe, H.: A curved multicomponent aerosol hygroscopicity model framework: Part 2 - Including organic compounds, Atmos. Chem. Phys., 5, 1223–1242, 2005b.

Vakeva, M., Hameri, K., and Aalto, P. P.: Hygroscopic properties of nucleation mode and Aitken mode particles during nucleation bursts and in background air, J. Geophys. Res., 107(D19), PAR9-1-11, 2002.

Varutbangkul, V., Brechtel, F. J., Bahreini, R., Ng, N. L., Keywood, M. D., Kroll, J. H., Flagan, R. C., Seinfeld, J. H., Lee, A., and Goldstein, A. H.: Hygroscopicity of secondary organic aerosols formed by oxidation of cycloalkenes, monoterpenes, sesquiterpenes, and related compounds, Atmos. Chem. Phys., 6, 2367–2388, 2006, http://www.atmos-chem-phys.net/6/2367/2006/.

Virkkula, A., Van Dingenen, R., Raes, F., and Hjorth, J.: Hygroscopic properties of aerosol formed by oxidation of limonene, alpha-pinene, and beta-pinene, J. Geophys. Res., 104, 3569–3579, 1999.

Zhou, J. C., Swietlicki, E., Berg, O. H., Aalto, P. P., Hameri, K., Nilsson, E. D., and Leck, C.: Hygroscopic properties of aerosol particles over the central Arctic Ocean during summer, J. Geophys. Res., 106, 32 111–32 123, 2001.